

DISTRIBUTED BRANCH POINTS AND THE SHAPE OF HYPERBOLIC SURFACES

TOBY L. SHEARMAN AND SHANKAR C. VENKATARAMANI[†]

ABSTRACT. We develop a theory for distributed branch points and investigate their role in determining the shape and influencing the mechanics of thin hyperbolic objects. We show that branch points are the natural topological defects in hyperbolic sheets, they carry a topological index which gives them a degree of robustness, and they can influence the overall morphology of a hyperbolic surface without concentrating energy. We develop a discrete differential geometric (DDG) approach to study the deformations of hyperbolic objects with distributed branch points. We present evidence for a quantitative version of Hilbert-Efimov theorem on the non-existence of twice differentiable isometric immersions of complete hyperbolic surfaces with uniformly negative curvature. Our result indicates how the maximum curvature should grow with the size of a hyperbolic domain immersed in \mathbb{R}^3 . We show that, to optimize norms of the curvature, i.e. the bending energy, distributed branch points are inevitable in sufficiently large hyperbolic surfaces. Further, they are distributed so that they lead to fractal-like recursive buckling patterns.

MSC: 53C42 (Primary) 53A70, 53C80, 35Q74, 74K99 (Secondary)

1. INTRODUCTION

Leaves, flowers, fins, wings and sails are examples of the ubiquity of thin sheets in natural and engineered structures. These objects often display intricate rippling and buckling patterns around their edges. Figure 1 displays some of the complex shapes of leaves and flowers that result from such hierarchical, “multiple-scale” buckling (See also [85, 87, 66, 88]). This phenomenon is not restricted to living organisms, where it might be explained as a genetic trait selected for by evolution; it is seen in torn plastic sheets [87]. Also, a wavy pattern can be induced in a naturally flat leaf; Sharon et al. show that application of the growth hormone auxin to the edge of an eggplant leaf, which is naturally flat, induces growth at the margin, ultimately causing buckling out of plane [85].

Qualitatively similar patterns are observed in torn plastic [86, 87] and temperature sensitive hydrogels [59, 55]. These patterns, and their bifurcations, have been studied intensively over the last 20 years [86, 70, 8, 59, 29, 60, 40], and it was recognized very early that these buckling patterns are a result of localized growth near the edge of a thin object [86]. The changes to the internal structure during the growth of a leaf or through

Date: April 5, 2022.

Key words and phrases. Pseudospherical immersions, discrete differential geometry, branch points, self-similar buckling patterns, extreme mechanics.

[†]Corresponding author.



FIGURE 1. (a) A leaf with regular undulations (photo by T Shearman) and (b) An Iris with 3 generations of undulations (photo by S Venkataramani).

the stretching of a plastic sheet at a tear result in surfaces whose intrinsic geometry (i.e. Riemannian metric [89]) are no longer “compatible” with a flat shape; significant external forces compressing the elastic sheet would need to be imposed for the surface to lay flat. The analogy between the localized stretching near the edge of a torn plastic sheet and the preferential growth of leaves along to their edge motivates the need for a purely mechanical explanation for the observed self-similar, fractal-like buckling patterns [70, 8, 87, 65, 30, 36].

Hydrogels have emerged as a useful system for exploring thin sheets with complex geometries in a controllable and reproducible manner [59, 28, 55]. Experimental techniques can prescribe a desired Riemannian metric in a hydrogel sheet that is initially flat, but acquires the programmed metric upon “activation” [59, 55, 56]. A variety of environmental stimuli, such as a shining light or temperature changes can activate the programmed metric. A gel sheet that swells more near the center leads to an ultimately spherical shape. Alternatively, if the differential swelling is larger near the margins and reproduces the effect seen in leaves, producing a wavy surface [59, 28, 50]. Hydrogels which undergo such controlled shape transitions, due to a switch in the metric, have a variety of potential applications in medical devices, micro- and nano-scale robotics and flexible electronics.

Another “experimental” system, less quantitative, but beautifully pairing art and mathematics is ‘hyperbolic crochet’ [46, 71, 96]. Through crochet, artists/mathematicians have rendered embeddings of (subsets of) the hyperbolic plane \mathbb{H}^2 in \mathbb{R}^3 . Hyperbolic crochet is constructed by increasing the perimeter exponentially with the radius. Sprawling hyperbolic crochet provides striking resemblance to sea creatures and plant life and has been exhibited through ‘The Crochet Coral Reef project’ [96]. In ‘Floraform’, a project inspired by the differential growth in plant structures and the ruffles of lettuce sea slugs, the authors simulate growth of a thin surface using techniques from differential geometry and physics, to uncover novel design principles and also to create art [68].

There is remarkable unity of form in leaves and hyperbolic hydrogels [50], in corals and crochet [96], in sea slugs and jewellery made using simulated differential growth [68]. Why is this so? This is the fundamental question we address in this paper – *Why do systems, with*

completely different physics, some directed by complex evolutionary processes and others generated by simple mathematical rules, end up with similar fractal-like buckling patterns?

A commonly held explanation is that hyperbolic surfaces, i.e. objects whose perimeter grows exponentially with the radius, develop complex buckling patterns because there are no smooth ways to embed them in \mathbb{R}^3 without stretching [46]. Putative evidence for this picture includes results that imply a dependence of the buckling wavelength on the thickness of the sheet [8, 60, 10, 93] suggesting a competition between localized stretching energy and regularization from bending energy. However, these scaling laws arise from (sometimes implicit) boundary or “forcing” conditions. There are no proofs (yet) that these scaling laws also apply to free sheets. Theorems on non-existence [47, 48] and singularities [3, 27] for isometric immersions of complete surfaces with negative curvature are sometimes invoked in this context. This argument, however, is a misunderstanding of the results in [47, 27] which apply to *complete* surfaces that are necessarily unbounded. Any finite piece of a smooth hyperbolic surface can always be smoothly and isometrically embedded in \mathbb{R}^3 [42].

As we argue in this paper, the answer is somewhat more subtle, and it is tied to the regularity of the allowed configurations of a hyperbolic sheet in \mathbb{R}^3 . In particular, we demonstrate that the class of $C^{1,1}$ isometric immersions (no stretching, uniformly bounded curvatures that are not necessarily continuous) are “flexible” while C^2 (continuous curvatures) isometric immersions are “rigid”. ‘Singular’ $C^{1,1}$ isometries can have substantially smaller elastic energy than ‘smooth’ C^2 isometries, which seems, on the surface, completely counter-intuitive. Further, the organizing principle for minimizing the energy of $C^{1,1}$ isometries is approximate “local” balance between the principal curvatures [36], and this naturally leads to fractal-like buckling patterns, as we show in this work.

The key to the flexibility of $C^{1,1}$ immersions is a novel topological defect in hyperbolic sheets, that we call a *branch point* [58, 38]. In §3, we show how we can use branch points to construct physically relevant $C^{1,1}$ isometries. We outline two distinct procedures, *assembly* (see §3.2) and *surgery* (see §3.3) for this construction. We also prove rigorous results that identify a natural topological charge, the order of saddleness m_p , that is associated with branch points. This topological charge makes branch points robust and precludes them from being smoothed away (Theorem 3.8). They also play a key role in extending the classical sine-Gordon equation for smooth pseudospherical surfaces to the larger class of $C^{1,1}$ branched pseudospherical surfaces (Theorem 3.13).

In §4 we review tools from discrete differential geometry (DDG) and apply them to $C^{1,1}$ pseudospherical immersions. We develop a DDG for branched Chebyshev nets in the Hyperbolic plane \mathbb{H}^2 (see §4.1). Existing DDG methods for pseudospherical immersions work with Chebyshev nets in S^2 and the corresponding A -nets in \mathbb{R}^3 [17] give an asymptotic parametric representations of pseudospherical surfaces. Our theory, on the other hand, directly represents the deformation, i.e. the Lagrangian to Eulerian map (Algorithm 4.1), the “mechanically relevant” description of a flexible sheet.

In §5 we study various aspects of branch points as they relate to applications. We present a scaling argument that allows us compute the energy and the number of wrinkles of hyperbolic disks embedded in \mathbb{R}^3 and compare the analytic predictions with numerical simulations. We also investigate the role of branch points in growing hyperbolic sheets,

and in conferring novel mechanical properties to thin hyperbolic sheets. We close with a short discussion of our results and potential future research directions in §6.

2. NON-EUCLIDEAN ELASTICITY

We model our elastic bodies as hyperelastic materials, so that the observed configurations are minimizers of an elastic energy functional. The functional quantifies the elastic energy due to strains in a particular deformed configuration of the body relative to the intrinsic (non-Euclidean) geometry which can be represented as a Riemannian manifold (\mathcal{B}, g) . This suggests a candidate for the resulting three-dimensional elastic energy

$$(2.1) \quad \mathcal{E}[y] = \int_{\mathcal{B}} \|\partial_i y \cdot \partial_j y - G_{ij}\|^2 dV,$$

with $y : \mathcal{B} \rightarrow \mathbb{R}^3$ representing the deformation [7, 70, 29]. Though Eq. (2.1) is arguably a prototypical model elastic energy, this functional is not appropriate from variational perspective [64] because of the possibility of fine-scale, orientation-reversing “folded structures”. A modification that removes this problem is to define the elastic energy using a polar decomposition of the deformation gradient ∇y to measure its deviation from an “energy well” corresponding to no stretching, $\mathcal{F}(x) = \{RA(x) : R \in SO(3)\}$, where $A = \sqrt{G}$ is the symmetric, positive definite root of the Riemannian metric G [64]. This defines the elastic energy

$$(2.2) \quad I[y] = \int_{\mathcal{B}} \text{dist}^2(\nabla y(x), \mathcal{F}(x)) dx.$$

The fully 3-dimensional variational problem for (2.1) is analytically intractable motivating the development of many asymptotically reduced models for shells, plates and rods [69, 9]. In the case of plates

$$\mathcal{B} = \Omega \times \left(-\frac{h}{2}, \frac{h}{2}\right), \quad G_{ij} = \begin{pmatrix} g_{11} & g_{12} & 0 \\ g_{21} & g_{22} & 0 \\ 0 & 0 & 1 \end{pmatrix},$$

the Föppl-von Kármán approximation [22, 34, 63] is one such asymptotic reduction of the full 3-dimensional system to a 2-dimensional system on the center-surface Ω in the limit of vanishing thickness $h \rightarrow 0$. Here and henceforth g will represent the 2d metric on Ω . Scaling the in- and out-of-plane displacements to be $O(\sqrt{h})$ and $O(h)$ respectively gives

$$(2.3) \quad \mathcal{E}^h = h \mathcal{E}_{\text{stretching}} + h^3 \mathcal{E}_{\text{bending}},$$

for a sheet of thickness h . The resulting variational formulation, also known as the Föppl-von Kármán (FvK) equations, are a collection of coupled partial differential equations representing the equilibrium conditions associated with the reduced energy and have been used extensively to model thin elastic sheets. Significant work has gone into rigorously justifying the FvK approximation. Ciarlet showed that solutions of FvK equations are equivalent to solutions of the leading order asymptotic expansion of the fully 3-dimensional energy for vanishing thickness in the case of a Euclidean reference metric [22]. This limit was rigorously justified by Friesecke et. al using Γ -convergence, and in fact they derive a

hierarchy of limiting elastic energy functionals that are distinguished by the scaling of the energy with respect to thickness [34, 35].

Efrati et al. extended the FvK theory to non-Euclidean plates, *i.e.* cases where the reference metric g is not the Euclidean metric [29]. Using the formalism in [29], the energy of an idealized isotropic material with elastic modulus Y and Poisson ratio $\nu = 0$ [9] is

$$(2.4) \quad \mathcal{E}^h = \frac{Yh}{2} \int \|dy \cdot dy - g\| dA + \frac{Yh^3}{24} \int (4H^2 - 2K) dA.$$

The first integral measures the stretching energy, quantifying the deviation of the induced metric from an assumed reference metric. The second integral, also known as the Willmore functional, describes the energy due to bending. H represents the mean curvature, $H = \frac{\kappa_1 + \kappa_2}{2}$ and K the Gauss curvature, $K = \kappa_1 \kappa_2$ where κ_1 and κ_2 are the two principal curvatures of the immersion $y : \Omega \rightarrow \mathbb{R}^3$.

The separation of scales in the thickness parameter $h \rightarrow 0$ leads to a distinct preference to use bending deformations to eliminate stretching entirely. Indeed, this is rigorously proven by Lewicka et al via Γ -convergence [64]. The limiting energy in the vanishing thickness limit [63, 64], after rescaling by $\frac{Yh^3}{24}$, is given by the Willmore energy restricted to isometries:

$$(2.5) \quad \frac{24h^{-3}}{Y} \mathcal{E}[y] \xrightarrow{\Gamma} \mathcal{E}_2[y] = \begin{cases} \int (\kappa_1^2 + \kappa_2^2) dA & \text{if } y \in W^{2,2}, dy \cdot dy \equiv g, \\ +\infty & \text{otherwise.} \end{cases}$$

In this work, we will also consider an alternative bending energy, the *max curvature* $\mathcal{E}_\infty[y] = \max_\Omega (|\kappa_1|, |\kappa_2|)$ for $y \in W^{2,\infty}$, $dy \cdot dy \equiv g$ and $+\infty$ otherwise. For all bounded domains, the limit (Willmore) energy \mathcal{E}_2 is bounded by (the square of) the \mathcal{E}_∞ , so finding configurations with \mathcal{E}_∞ finite is sufficient for showing the existence of finite Willmore energy isometries.

A significant obstruction to finding these configurations is the *singular edge*, observed, for instance, in the classical pseudosphere; see Figure 2. The singular edge is an example of a *cuspidal edge singularity*, and is a generic feature of smooth isometric immersions of \mathbb{H}^2 into \mathbb{R}^3 [3, 52]. One of the principal curvatures diverges at the singular edge so the $W^{2,\infty}$ energy is locally unbounded. As we show elsewhere, the Willmore energy also diverges in any neighborhood of a point on the singular edge. Our principal concern in this work will therefore be the question of how to evade or stave off the occurrence of a singular edge.

The question of isometric embeddings and immersions of a Riemannian 2-manifold (Ω, g) as a surface in \mathbb{R}^3 has a long history, reviewed in [42]. We are specifically interested in the case of hyperbolic surfaces, *i.e.* when g has negative intrinsic Gauss curvature [89]. In 1901, Hilbert showed that there exists no geodesically complete, analytic immersion into \mathbb{R}^3 of a metric with constant negative curvature [47]. This result was later extended by Efimov to C^2 isometries for any metric with negative curvature bounded away from zero [26, 72]:

Theorem (Efimov). *No surface with negative Gauss curvature bounded away from zero $K \leq -\delta < 0$ can be C^2 immersed in Euclidean 3-space so as to be complete in the induced Riemannian metric.*

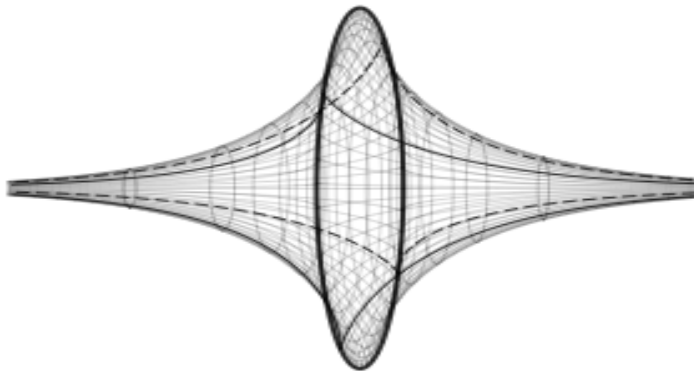


FIGURE 2. An example of the singular edge occurring in the classical pseudosphere.

Alternatively, Nash [74] and Kuiper [62] showed that, for a general metric g , there exists a C^1 isometric immersion, indeed even an embedding:

Theorem (Nash-Kuiper). *Let (\mathcal{M}, g) be an m -dimensional Riemannian manifold and $f : \mathcal{M} \rightarrow \mathbb{R}^n$ a short immersion (resp. embedding), where $n \geq m + 1$. Given an $\epsilon > 0$, there exists an isometric immersion (resp. embedding) f_ϵ of class C^1 satisfying*

$$(2.6) \quad g(v, w) = \langle df_\epsilon(v), df_\epsilon(w) \rangle,$$

which is uniformly ϵ -close to f in the Euclidean norm on \mathbb{R}^n :

$$(2.7) \quad \|f(x) - f_\epsilon(x)\| < \epsilon \text{ for all } x \in \mathcal{M}.$$

The juxtaposition of these two results provides a strong motivation to explore isometric immersions with regularities between C^1 and C^2 . In the context of the Nash-Kuiper theorem, the metric g may be arbitrary with the guarantee of a C^1 isometry. However, an immersion needs to be at least weakly twice differentiable in order to define curvatures and bending energy. The surface must be of class $W^{2,2}$ for the bending content to be finite. Therefore $W^{2,2}$ is the natural space of immersions to explore, as is clear from the reduced energy (2.5). Provided that the space of $W^{2,2}$ -isometric immersions is nonempty, containing potentially many immersions, we use the elastic energy as a selection process: the observed surface is the isometric immersion which minimizes the bending energy.

Remark 2.1. Bella and Kohn prove that wrinkles do arise through a competition between stretching and bending energies, for $h > 0$, with additional “forcing” conditions that restrict the class of allowed deformations [10, Thm. 1]. In this circumstance, the $W^{2,2}$ energy of the minimizers does not stay bounded as $h \rightarrow 0$, i.e. the limiting isometries are not $W^{2,2}$.

We consider a different scenario in this work, namely *free sheets* with no imposed forces or boundary conditions. To analyze equilibrium states we have to impose boundary conditions that are appropriate for isometric immersions of free sheets, namely zero net forces

and moments [41]. In this work, we take a variational perspective for the problem of minimizing (2.5), or the simpler problem of minimizing $\mathcal{E}_\infty = \kappa_{\max}$. Our candidate states are therefore “test functions” for the energy and, unlike equilibria, they need neither satisfy the appropriate Euler-Lagrange equations nor the corresponding boundary conditions.

3. HYPERBOLIC SURFACES WITH BRANCH POINTS

The preceding discussion highlights the role of the *regularity* of isometries. Beyond the existence/non-existence of isometries, it is crucial whether a candidate isometry is in $W^{2,2}$. This motivates the problem: (Ω, g) is a Riemannian 2-manifold.

$$(3.1) \quad \text{Find } y : \Omega \rightarrow \mathbb{R}^3 \text{ such that } y \in W_{\text{loc}}^{2,2}(\Omega, \mathbb{R}^3), \quad dy \cdot dy = g \text{ a.e.}$$

If $y : \Omega \rightarrow \mathbb{R}^3$ is C^1 , the Gauss Normal map is given by $N = \frac{\partial_1 y \times \partial_2 y}{\|\partial_1 y \times \partial_2 y\|}$ with $\partial_i = \frac{\partial}{\partial x^i}$ for (arbitrary) coordinates (x^1, x^2) on Ω . If y and g are C^2 , it follows that N is C^1 and Gauss’ *Theorema Egregium* implies that (3.1) is equivalent to the Monge-Ampere Exterior differential system (EDS) [53, §6.4]:

$$(3.2) \quad N \cdot dy = 0, \quad N^*(d\Omega) = \kappa dA, \quad \kappa \equiv \kappa[g] \text{ is determined by } g,$$

where $d\Omega$ is the area form on the sphere S^2 and κ is the Gauss curvature.

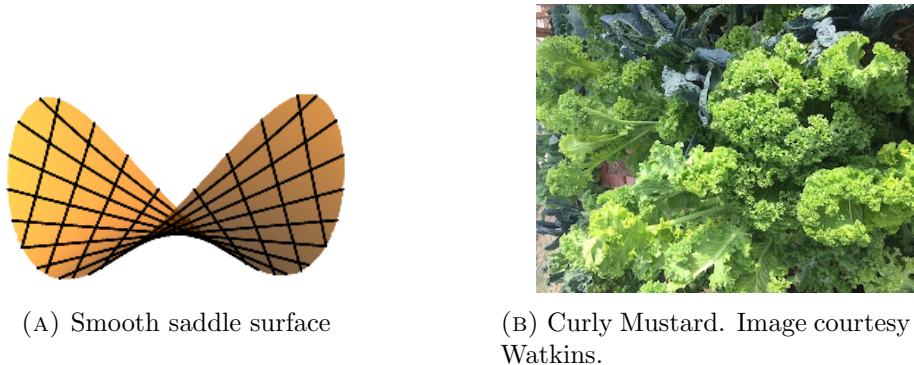


FIGURE 3. Hyperbolic surfaces in \mathbb{R}^3 .

Classical results in differential geometry imply that smooth solutions of (3.2) with $\kappa < 0$ are hyperbolic surfaces and locally saddle shaped. In contrast, the curly mustard leaf in Fig. 3b is “frilly”, i.e buckled on multiple scales with a wavelength that refines (“sub-wrinkles”) near the edge [85]. This “looks” very unlike the smooth saddle in Fig. 3a. If $\Omega \subset \mathbb{R}^2$ is a bounded domain with a smooth boundary, and g is a smooth metric on Ω with negative curvature, g can be extended to a smooth metric \bar{g} on \mathbb{R}^2 with Gauss curvature $\kappa[\bar{g}] < 0$ decaying (as rapidly as desired) at infinity. The existence of isometric immersions into \mathbb{R}^3 , of smooth metrics with decaying negative curvature [49], therefore implies that bounded smooth hyperbolic surfaces can be smoothly and isometrically embedded in \mathbb{R}^3 . A smooth (C^2 is sufficient) hyperbolic surface cannot refine its buckling pattern and is

thus “non-frilly”, as we show in §3.2. Why do we see frilly shapes in natural surfaces, as in Fig. 3b, rather than the smooth saddles of Fig. 3a?

We have addressed aspects of this puzzle in recent work [38, 39, 40, 36, 2] and the short answer is that, for a given metric g , the frilly surfaces, somewhat counterintuitively, can have *smaller* bending energy than the smooth saddle, despite being (seemingly) rougher. It is true that C^2 hyperbolic surfaces are saddle-like near every point. A key result in this work is the identification of a topological invariant, the winding number (ramification index) of the normal map at a branch point, that distinguishes sub-wrinkled surfaces from saddles locally (See Lemma 3.6). With branch points, the surfaces are only $C^{1,1}$, but gain the additional flexibility to refine their buckling pattern and thus lowering their energy [36]. This flexibility *is not available* to smooth saddles, and constitutes a key property of surfaces with branch points [36].

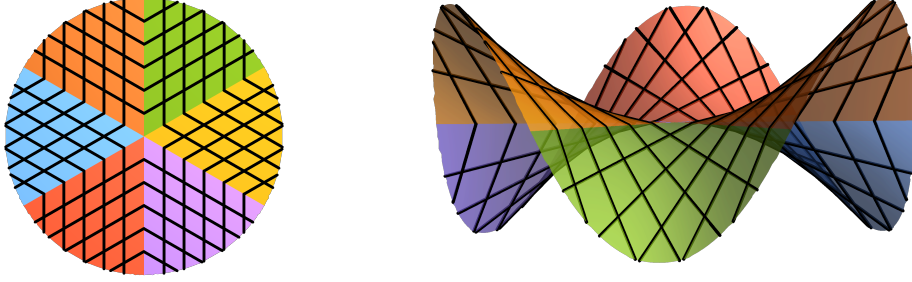
The additional flexibility for $C^{1,1}$ immersions of hyperbolic surfaces has been explored since the 1960s. Rozendorn discussed the branched hyperbolic paraboloid as an important example of a $C^{1,1}$ hyperbolic surfaces [83], and constructed $C^{1,1}$ immersions of geodesically complete, uniformly negatively curved ($K \leq -\delta < 0$) surfaces that are smooth except at finitely many points [80, 82, 83].

Some aspects of this increased flexibility of $C^{1,1}$ surfaces are illuminated by the following “reduced” model. The hyperbolic Monge-ampere equation $\det(D^2w) = -1$ admits smooth solutions given by quadratic functions. Figure 4 shows the construction of a non- C^2 solutions – a branched hyperbolic paraboloid obtained from the smooth quadratic solution $w = \frac{1}{2} \left(\frac{x_1^2}{\sqrt{3}} - \sqrt{3}x_2^2 \right)$. Cutting out the sector $|x_1| \leq \sqrt{3}|x_2|$ and then patching congruent copies of this sector by odd reflections gives a $W^{2,2}$ surface with a continuous normal vector and bounded curvature [83, 38]. The “defects” in this surface include the point in the middle – a *branch point* and the 6 rays through this point – *lines of inflection*, which together constitute an *asymptotic skeleton* for the surface, as we discuss in §3.4.

Note that, on the sector $|x_1| \leq \sqrt{3}|x_2|$, we have $w = \frac{1}{2\sqrt{3}}(x_1 + \sqrt{3}x_2)(x_1 - \sqrt{3}x_2)$ is a product of two linear factors with real coefficients, so the surface $(x_1, x_2, w(x_1, x_2))$ is ruled. Indeed the lines of constant $x_1 \pm \sqrt{3}x_2$ will map into straight lines on the solution surface. This property of being a ruled surface is preserved by rigid Euclidean motions, so it follows that the patched surface is also ruled, although the directions of the rulings will, in general, be different in different sectors (see Fig. 4).

This construction can be extended to generate $C^{1,1}$ hyperbolic surfaces with multiple distinct branch points, and an interesting question is how these defects interact with and influence each other [36]. In contrast to Rozendorn’s construction, where the focus was on keeping the curvature negative, rather than preserving a particular metric, and minimizing the “singular set” of $C^{1,1}$ points, the constructions in [36, 38] exactly preserve the metric, and introduce the $C^{1,1}$ points to achieve other goals, including enlarging the domain that can be immersed isometrically, and optimizing the bending energy over isometries.

3.1. Pseudospherical surfaces. We will build constant negative curvature branched $C^{1,1}$ surfaces by patching together C^2 immersions of subsets of \mathbb{H}^2 , such that the pieces join



(A) Six $\pi/3$ sectors in the unit disk. (B) A piecewise quadratic hyperbolic surface.

FIGURE 4. A $W^{2,2}$ solution of $\det(D^2w) = -1$ built by patching together (smooth) quadratic solutions on the 6 sectors shown in (a). The straight lines in the surface (b) are the images of the straight lines in the unit disk (a). The existence of such straight lines is a consequence of each sector being a piece of a doubly ruled parabolic hyperboloid.

with continuous tangent planes. To this end, we collect and also extend a few properties of C^2 pseudospherical surfaces (See [31, Chaps. V & VI] [79, §1.1 & §1.2] and [25]).

- (A) Every C^2 immersion with $K = -1$ admits a pair of asymptotic coordinates (u, v) (locally) so that parametrized surface $(u, v) \mapsto r(u, v)$ satisfies $r_u \times r_v \neq 0, N \cdot r_{uu} = N \cdot r_{vv} = 0$ where $N = \pm r_u \times r_v / \|r_u \times r_v\|$ [44]. The sign choice in the definition of N is immaterial if $\|r_u \times r_v\|$ never vanishes.
- (B) By the Beltrami-Enneper theorem [31, Chap. V], the unit-speed asymptotic curves $r(\cdot, v_0)$ and $r(u_0, \cdot)$ have constant torsions ± 1 . We choose the u and v coordinates so that the corresponding asymptotic curves have torsions -1 and $+1$ respectively. Since $r_u \perp N$ and $r_v \perp N$, $(r_u, N \times r_u, N)$ is an orthonormal Frenet frame for the u -asymptotic lines $r(\cdot, v_0)$ and $(r_v, N \times r_v, N)$ is a frame for the v -asymptotic lines. The Frenet-Serret formulae [31, Chap. V] read

$$(3.3) \quad \begin{aligned} \partial_u \begin{pmatrix} r_u \\ N \times r_u \\ N \end{pmatrix} &= \begin{pmatrix} 0 & \kappa^u & 0 \\ -\kappa^u & 0 & -1 \\ 0 & 1 & 0 \end{pmatrix} \begin{pmatrix} r_u \\ N \times r_u \\ N \end{pmatrix}, \\ \partial_v \begin{pmatrix} r_v \\ N \times r_v \\ N \end{pmatrix} &= \begin{pmatrix} 0 & \kappa^v & 0 \\ -\kappa^v & 0 & 1 \\ 0 & -1 & 0 \end{pmatrix} \begin{pmatrix} r_v \\ N \times r_v \\ N \end{pmatrix}. \end{aligned}$$

κ^u and κ^v are the geodesic curvatures of the u and v asymptotic lines.

- (C) The Frenet-Serret equations yield $N_u = N \times r_u$ so (r_u, N_u, N) is a right-handed orthonormal frame. Similarly, $(r_v, -N_v, N)$ is a right-handed orthonormal frame. This gives the *Lelievre formulae* [79]

$$(3.4) \quad \begin{aligned} r_u(u, v) &= N_u(u, v) \times N(u, v), \\ r_v(u, v) &= -N_v(u, v) \times N(u, v). \end{aligned}$$

- (D) The Lelievre equations are consistent if and only if $\partial_v(r_u) = \partial_u(r_v)$ which is equivalent to the condition that the normal field $(u, v) \mapsto N(u, v)$ is *Lorentz harmonic*

$$(3.5) \quad N \times N_{uv} = 0.$$

It immediately follows that $r_{uv} = N_u \times N_v$.

- (E) Note that Eqs. (3.4) and (3.5) and the signs of the torsions in (3.3) are invariant under three separate symmetries, $N \rightarrow -N, u \rightarrow -u$ or $v \rightarrow -v$. Also, the transformations $u \rightarrow -u, v \rightarrow -v$ or $N \rightarrow -N$, respectively, reverse the sign of the geodesic curvature κ^u , reverse the sign of κ^v , and reverse the signs of both κ^u and κ^v in (3.3).
- (F) Note that $-u$ (resp. $-v$) is as much a valid asymptotic coordinate as is u (resp. v). This is not an issue with global (smooth) asymptotic coordinates, but will be an issue for the branched surfaces that are our principal objects of interest.

We will define N so that it is continuous in situations where the underlying surface is C^1 , *independent of the specific asymptotic parametrization*. Let ω be an orientation (a non-vanishing 2 form) on this surface. If the surface is a graph $(x_1, x_2, w(x_1, x_2))$, a canonical choice is $\omega = dx_1 \wedge dx_2$. We define the normal N so that the orientation ω on the surface is consistent with the cross product in the ambient space \mathbb{R}^3 i.e. $\omega(X, Y) = \beta(X \times Y) \cdot N$ for all vector fields X, Y tangential to the surface and a strictly positive function β . This is equivalent to defining

$$N \equiv N_\omega = \text{sign}(\omega(r_u, r_v)) \frac{r_u \times r_v}{\|r_u \times r_v\|} = \sigma \frac{r_u \times r_v}{\|r_u \times r_v\|}$$

where we have defined $\sigma \equiv \text{sign}(\omega(r_u, r_v))$ to keep the notation compact. It is easy to see that this definition of N is insensitive to “flips” $u \rightarrow -u$ or $v \rightarrow -v$ in the asymptotic parametrization. A related issue is addressed in the definition of the normal N_{front} for a *pseudospherical front* in Ref. [25], where the consideration was the potential vanishing of $\|r_u \times r_v\|$.

- (G) If we define the angle between the asymptotic directions by $\cos \varphi = r_u \cdot r_v$, this definition is not invariant under the flips $u \rightarrow -u$ or $v \rightarrow -v$. We therefore pick an “invariant” definition for the angle between the asymptotic directions by

$$(3.6) \quad \begin{aligned} \cos(\varphi) &= \sigma r_u \cdot r_v = -\sigma N_u \cdot N_v, \\ \sin(\varphi) &= \sigma (r_u \times r_v) \cdot N \\ &= \|r_u \times r_v\| \\ r_{uv} &= N_u \times N_v = -\sigma \sin \varphi N \end{aligned}$$

For this definition, $\sin \varphi \geq 0$ so $0 \leq \varphi \leq \pi$. r is an immersion only if r_u and r_v are linearly independent, so this precludes φ from attaining the values 0 or π on a smooth pseudospherical surface. Initially, we work on open sets where $\omega(r_u, r_v)$ does not change sign and $\|r_u \times r_v\|$ is nonvanishing.

(H) In terms of this angle φ and the normal $N = N_\omega$, the first and second fundamental forms of the pseudospherical surface are given by

$$(3.7) \quad \begin{aligned} g &= dr \cdot dr = du^2 + 2\sigma \cos \varphi \, dudv + dv^2 \\ h &= dN_\omega \cdot dr = -2\sigma \sin \varphi \, dudv \end{aligned}$$

(I) $N_u = N \times r_u$ and $N_v = -N \times r_v$ are in the plane perpendicular to N that is spanned by r_u, r_v . Indeed N_u is obtained by rotating r_u by $\pi/2$ and N_v is r_v rotated by $-\pi/2$. Differentiating, and using (3.6), we get

$$(3.8) \quad \begin{aligned} N_{uv} &= N_v \times r_u = -(N \times r_v) \times r_u \\ &= N(r_u \cdot r_v) - r_v(r_u \cdot N) = \sigma \cos \varphi N = -(N_u \cdot N_v)N \end{aligned}$$

(J) To extract all the compatibility conditions encoded in (3.3), we also need the derivatives of the Frenet frame for the u -lines with respect to v and vice versa. Recognizing that $N \times r_u = N_u$ and combining the results in the previous items, we have

$$\partial_v \begin{pmatrix} r_u \\ N \times r_u \\ N \end{pmatrix} = \sigma \begin{pmatrix} 0 & 0 & -\sin \varphi \\ 0 & 0 & \cos \varphi \\ \sin \varphi & -\cos \varphi & 0 \end{pmatrix} \begin{pmatrix} r_u \\ N \times r_u \\ N \end{pmatrix}.$$

Writing these equations abstractly as $\partial_u F^u = AF^u$, $\partial_v F^u = BF^u$, where F^u denotes the frame (r_u, N_u, N) , compatibility $\partial_v(\partial_u F^u) = \partial_u(\partial_v F^u)$ is equivalent to the *zero-curvature condition* $\partial_v A - \partial_u B + [A, B] = 0$ [79, 17]. Computing the matrix entries for this system, and the corresponding system for the frame F^v , we get

$$(3.9) \quad \begin{aligned} \kappa^u &= -\partial_u \varphi, \quad \kappa^v = \partial_v \varphi, \\ -\partial_v(\kappa^u) &= \partial_u(\kappa^v) = \varphi_{uv} = \sigma \sin \varphi, \end{aligned}$$

the *Sine-Gordon equation* for φ and relations between the geodesic curvatures κ^u, κ^v of the asymptotic curves and the derivatives of φ . In obtaining this equation, we have assumed that σ is a constant, so this only applies to open sets where $\omega(r_u, r_v)$ does not change sign. In §3.5 we generalize the Sine-Gordon equation to situations where σ can change sign (see Theorem 3.13).

We are now in position to define the basic building block of a branched pseudospherical surface. We will follow the discussion in Ref. [25]:

Definition 3.1. A function $(u, v) \mapsto f(u, v) \in \mathbb{R}^n$ is C^{1M} if each component is C^1 , and has continuous mixed partial derivatives $f_{uv} = f_{vu}$ on the domain of f .

Note that C^{1M} functions are not necessarily C^2 and neither f_{uu} nor f_{vv} needs to exist. Also, a smooth reparametrization $(u, v) = g(r, s)$ of a C^{1M} function f can yield a function $h(r, z) = f \circ g(r, s)$ that is *not* C^{1M} [25].

Definition 3.2. A C^{1M} mapping $N : D \rightarrow S^2$ is *weakly (Lorentz) harmonic* if

- (1) $N_u \cdot N_u > 0$ and $N_v \cdot N_v > 0$ on D .
- (2) N is *Moutard*, i.e. there is a continuous function $\nu : D \rightarrow \mathbb{R}$ such that $N_{uv} = N_{vu} = \nu N$ (cf. [17, Thm. 1.12]).

Weakly harmonic mappings $D \rightarrow S^2$ allows us to generalize the class of smooth pseudospherical surfaces [25]. In particular, if $N : D \rightarrow S^2$ is weakly harmonic, then there is a corresponding *pseudospherical front*, or PS-front for short [25], i.e. a C^{1M} solution $r : D \rightarrow \mathbb{R}^3$ to the Lelievre equations (3.4), that is weakly regular, i.e. $r_u \cdot r_u > 0, r_v \cdot r_v > 0$. PS-fronts allow for the possibility of singularities, i.e. sets where r is not an immersion, and a classical example is the singular edge of a pseudosphere (see Fig. 2 and also [25, §6]).

We also have a necessary and sufficient condition for ruling out such singularities – r is an immersion at every point where N is an immersion, i.e $N_u \times N_v \neq 0$ [25].

Definition 3.3. An *asymptotic sector* is a parametrized (not necessarily smooth) surface given by a mapping $r \in C^{1M}(K, \mathbb{R}^3) \cap C(\bar{K}, \mathbb{R}^3)$ that arises from solving the Lelievre equations (3.4) for a weakly harmonic mapping $N : K \rightarrow S^2$ where $K = (u_0, \infty) \times (v_0, \infty)$ (WLOG we can take K to be the positive quadrant). An *asymptotic quadrilateral* or *asymptotic rectangle* is an asymptotic sector restricted to a rectangular domain $(u_0, u_1) \times (v_0, v_1) \subset \mathbb{R}^2$.

3.2. Assembling a pseudospherical surface with branch points. As a first illustration of the procedure to construct $C^{1,1}$ isometric immersions of a prescribed hyperbolic metrics, we construct a monkey saddle with constant negative curvature, $K = -1$. Fix a constant $L > 0$ and an even integer $2m \geq 4$. The number $2m$ determines the number of asymptotic rays extending from the origin and the resulting topological structure of the asymptotic coordinate system.

Choose a set of angles $\alpha_i \in (0, \pi)$, $i \in \{0 \dots 2m - 1\}$ satisfying $\sum_i \alpha_i = 2\pi$. Let $\beta_0 = 0, \beta_i = \beta_{i-1} + \alpha_{i-1}$ for $i = 1, 2, \dots, 2m$, so that $0 = \beta_0 < \beta_1 < \beta_2 < \dots < \beta_{2m-1} < \beta_{2m} = 2\pi$. Also, we define the set of unit vectors $\mathbf{s}_i = \cos(\beta_i)\mathbf{e}_1 + \sin(\beta_i)\mathbf{e}_2$ and their “dual” vectors $\mathbf{s}_i^* = \mathbf{e}_3 \times \mathbf{s}_i = -\sin(\beta_i)\mathbf{e}_1 + \cos(\beta_i)\mathbf{e}_2$. Finally, we define the sectors $S_i \subset \mathbb{R}^2, i = 1, 2, \dots, 2m$ to be the convex cones generated by \mathbf{s}_{i-1} and \mathbf{s}_i , i.e., for $k = 1, 2, \dots, n$,

$$(3.10) \quad \begin{aligned} S_{2k-1} &= \{u_{k-1}\mathbf{s}_{2k-2} + v_k\mathbf{s}_{2k-1} \mid u_{k-1} \geq 0, v_k \geq 0\}, \\ S_{2k} &= \{u_k\mathbf{s}_{2k} + v_k\mathbf{s}_{2k-1} \mid u_k \geq 0, v_k \geq 0\}, \end{aligned}$$

distinguishing the “odd” and “even” sectors.

These definitions also define (u, v) coordinates on \mathbb{R}^2 . For any $\mathbf{x} \in \mathbb{R}^2$ let $u = u_k$ if $\mathbf{x} \in S_{2k} \cup S_{2k+1}$ and $v = v_k$ if $\mathbf{x} \in S_{2k-1} \cup S_{2k}$, so each coordinate is “good for 2 sectors”. The (u, v) coordinates are well-defined, since, on sets of the form $S_{2k-1} \cap S_{2k}$, where we might potentially have two definitions of u , we instead have $S_{2k-1} \cap S_{2k} = \{v\mathbf{s}_{2k-1} \mid v \geq 0\}$ so both choices, $u = u_{i-1}$ and $u = u_i$ give $u = 0$. Likewise, on sets of the form $S_{2k} \cap S_{2k+1}$, we have $v = 0$. We can determine these coordinates using the dual vectors \mathbf{s}_i^* as

$$(3.11) \quad (u, v) = \begin{cases} \frac{1}{\mathbf{s}_{2k-1}^* \cdot \mathbf{s}_{2k-2}} (\mathbf{s}_{2k-1}^* \cdot \mathbf{x}, -\mathbf{s}_{2k-2}^* \cdot \mathbf{x}) & \mathbf{x} \in S_{2k-1} \\ \frac{1}{\mathbf{s}_{2k-1}^* \cdot \mathbf{s}_{2k}} (\mathbf{s}_{2k-1}^* \cdot \mathbf{x}, -\mathbf{s}_{2k}^* \cdot \mathbf{x}) & \mathbf{x} \in S_{2k} \end{cases}$$

Clearly, u and v are not smooth across sectors. Rather, they are piecewise linear. Given a point $\mathbf{z} \in \mathbb{R}^3$, a direction $\mathbf{n} \in S^2$ and unit vectors \mathbf{e}_u and \mathbf{e}_v that are perpendicular to \mathbf{n} ,

we define the boundary conditions for an *Amsler sector* by

$$\begin{aligned}
 N(u, 0) &= \cos(u)\mathbf{n} + \sin(u)\mathbf{n} \times \mathbf{e}_u \\
 N(0, v) &= \cos(v)\mathbf{n} - \sin(v)\mathbf{n} \times \mathbf{e}_v \\
 (3.12) \quad r(u, 0) &= \mathbf{z} + u\mathbf{e}_u, \quad r(v, 0) = \mathbf{z} + v\mathbf{e}_v
 \end{aligned}$$

It is straightforward to verify that the definitions in (3.12) are solutions of (3.3). It follows that we can solve the Moutard equation (3.8) for the normal $N(u, v)$ (see [17, Thm 1.12] for the details) to obtain smooth solutions in the interior of the sector $\{u > 0, v > 0\}$ that extend continuously to the boundary $\{u \geq 0, v = 0\} \cup \{u = 0, v \geq 0\}$, where they agree with the definitions in (3.12).

We specialize by setting $\mathbf{z} = 0, \mathbf{n} = \mathbf{e}_3, \mathbf{e}_u = \mathbf{s}_{2k}$ on $S_{2k} \cup S_{2k+1}$ and $\mathbf{e}_v = \mathbf{s}_{2k-1}$ on $S_{2k-1} \cup S_{2k}$. Note that, for points that are in multiple sectors, i.e. points where either u or v is zero, N and r are defined consistently, i.e. they are same independent of which sector is taken in the definition. In particular, the point $u = v = 0$, which belongs to all sectors, has $r_i(0, 0) = \mathbf{z} = 0, N_i(0, 0) = \mathbf{n} = \mathbf{e}_3$ for all i .

In the interior of each sector S_i , the normal field N_i which solves the Moutard equation (3.8) is weakly harmonic and thus determines a PS-front $r_i : S_i \rightarrow \mathbb{R}^3$ through the Lelievre equations (3.4). Since $\lim_{(u,v) \rightarrow (0,0)} N_u \times N_v = \pm \mathbf{s}_{i-1}^* \times \mathbf{s}_i^* \neq 0$, it follows that there exist $c_i > 0$ such that $N_u \times N_v$ does not vanish on the rectangular domain $J_i \equiv \{0 < u < c_i, 0 < v < c_i\} \subset S_i$. r_i extends continuously to \bar{J}_i and (after translating $r_i \rightarrow r_i - \mathbf{z}$ if needed) we have constructed an asymptotic quadrilateral $r_i \in C^\infty(J_i) \cap C(\bar{J}_i)$ such that $r_i(0, 0) = 0$ and the normal to the immersion is given by our choices for N above, i.e. for points in $S_i \cap S_j$, N is well defined since the two potential definitions of the normal, N_i and N_j , agree.

This procedure is illustrated in Fig. 5 with $2m = 6, \alpha_k = \pi/3, k = 1, 2, \dots, 6$. Since the resulting immersion is continuous and piecewise smooth, and has a continuous and piecewise smooth normal field, it follows that the normal field is (globally) Lipschitz, and the immersion is $C^{1,1}$. The immersion restricted to each sector is an example of an *Amsler sector* [3], an object that will play a key role in our constructions below.

Indeed, we did not use any of the specific properties of Amsler sectors in our construction of a branched pseudospherical surface, and it is straightforward to generalize this construction, as we record in the following proposition.

Proposition 3.4 (Assembly). *The sectors $S_k, k = 1, 2, \dots, 2m$ and the (per sector) coordinates (u, v) are as defined above. Let $F_k : [0, c_k] \rightarrow \mathbb{R}^3$ be smooth Frenet frames for u and v asymptotic curves satisfying (3.3) with the initial conditions $N_k(0) = \mathbf{e}_3$ and $r_u(0) = \mathbf{s}_k$ or $r_v(0) = \mathbf{s}_k$ depending on whether k is even or odd. Then, we can construct $2m$ PS-fronts $r_k : S_k \rightarrow \mathbb{R}^3$ such that r_k is smooth in the interior of S_k and limits to the prescribed asymptotic curves with frames F_{k-1} and F_k at the boundaries of S_k . There is a neighborhood of the origin where (the piecewise defined) map $y : \Omega \rightarrow \mathbb{R}^3$, obtained by patching the maps r_k , and its normal N are immersions, y is $C^{1,1}$, and N is Lipschitz.*

The proof of this proposition is by explicit construction, in exactly the same manner as the argument from above. The prescribed data give the normal field N at the boundaries of

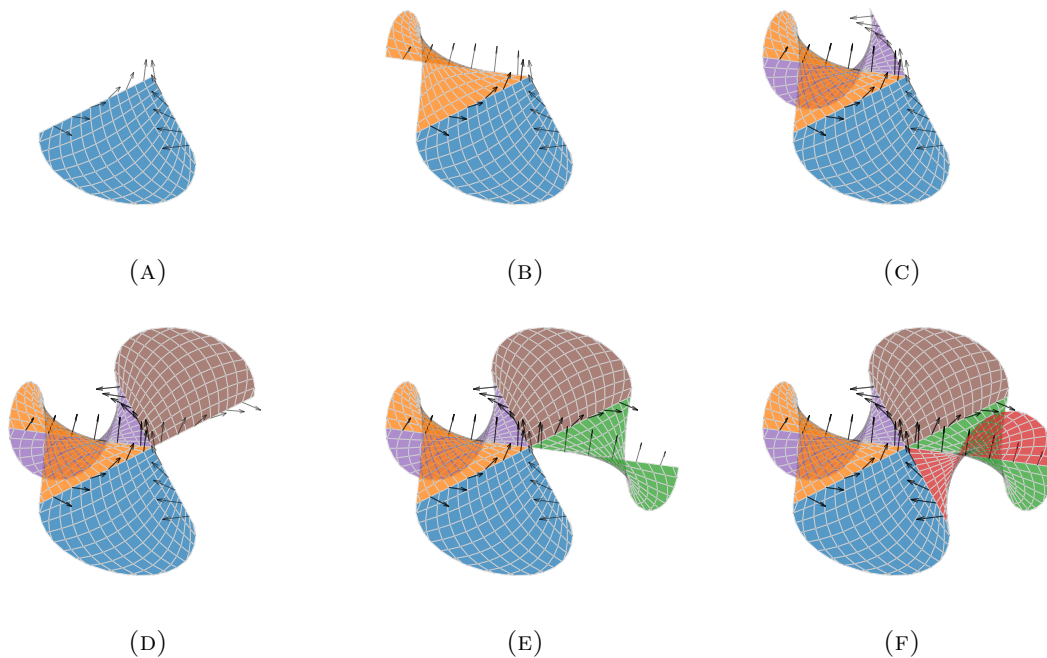


FIGURE 5. Construction of a $K = -1$ monkey saddle of geodesic radius 1. Each colored sector is smooth, and the gluing procedure maintains continuity of the normal field. The normal field is shown by the arrows.

the sectors, and we can solve (3.8) in the interiors to get a piecewise smooth, globally Lipschitz normal field N . This normal is weakly harmonic on each sector so we can construct the corresponding immersions using the Lelievre formulae.

The resulting surface is a saddle of order m , so a regular saddle is a saddle of order 2. The *order of saddleness* m_p at any point p in a saddle surface is the number of times any sufficiently small deleted neighborhood of p crosses from one side of (say “below”) the tangent plane at p to the other side (“above”) [81]. m_p thus measures the number of ‘undulations’ at p . The $m_p - 2$ “excess” undulations, in comparison with a regular saddle, persist all the way to the boundary. This is the mechanism through which branch points refine the buckling pattern as we approach the boundary of a hyperbolic surface.

For the point p , that is common to all the sectors S_k in Prop. 3.4, the order of saddleness $m_p = m$, corresponding to half the number of sectors at p . Since the asymptotic directions at p are defined by the intersection between the surface and the tangent plane at p [89], this relation, between the number of asymptotic directions at p and m_p holds more generally. This is illustrated in Figs. 6a and 6c. Every point in Fig. 6a has $m = 2$. In Fig. 6c, most points have $m = 2$ but there is one point with $m = 3$.

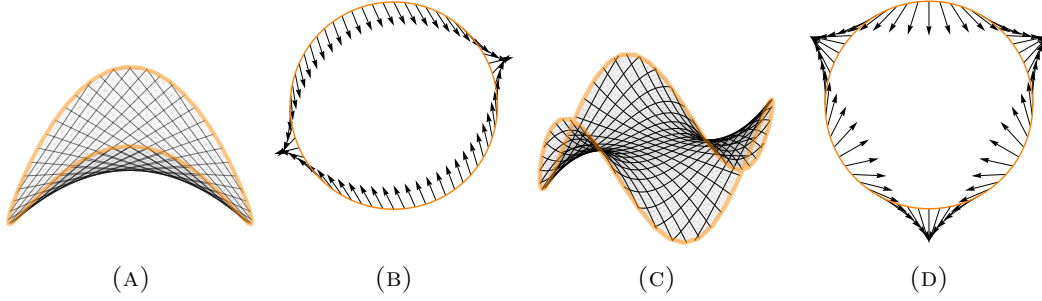


FIGURE 6. The (local) winding number of the normal field about a point p for two surfaces: (a) A smooth pseudospherical saddle and (c) A $C^{1,1}$ pseudospherical monkey saddle. (b),(d) Projections of the corresponding normal fields. p denotes the center of the disks. $m_p = 2, J_p = -1$ for the saddle and $m_p = 3, J_p = -2$ for the monkey saddle.

Let p be a point on the surface that is common to $2m$ sectors bounded by asymptotic curves. The sum of the angles of the sectors at p (in the surface) is clearly 2π . The images of these sectors under the Gauss normal map N , however, can wind around the normal $N(p)$ *multiple times*, as depicted in Fig. 6d. This motivates the definition of J_p , the degree of branching at a point p , by setting J_p equal to the local degree of the Gauss Normal map $x \mapsto N(x)$ in a deleted neighborhood of p . For surfaces with negative extrinsic curvature, $J_p < 0$ everywhere since the normal winds clockwise for a counterclockwise circuit around p . If $J_p = -1$, the normal map is a local homeomorphism. However, if $J_p < -1$, then $N(V)$ is a branched (“multiple-sheeted”) covering of a neighborhood of $N(p)$, which is therefore a branch point for the inverse of the Gauss normal map. We will, with a slight abuse of terminology, call p a branch point if $|J_p| > 1$, in keeping with standard usage [58, 40, 36].

Definition 3.5. $p \in V$, an open set and $U = V \setminus \{p\}$ is a deleted neighborhood of p . $N : V \rightarrow S^2$ is a continuous map with the property that $N(U) \subseteq S^2 \setminus \{\pm N(p)\}$, where $-N(p)$ is the antipodal point to $N(p)$. Since there is a canonical retraction $\pi : S^2 \setminus \{\pm N(p)\} \rightarrow S^1$ (“retracting to the equator”) we can define a topological invariant J_p , the *ramification index of the normal map*, as the degree of the (composite) map

$$S^1 \xrightarrow{\gamma} U \xrightarrow{N} S^2 \setminus \{\pm N(p)\} \xrightarrow{\pi} S^1,$$

where γ is a simple closed curve in U , $\pi(x) = x_\perp / \|x_\perp\|$ and $x_\perp = x - \langle N(p), x \rangle N(p)$.

The surface can be (locally) expressed as a graph $(x_1, x_2, w(x_1, x_2))$ where (x_1, x_2) are coordinates in the tangent plane at p , and $w(x_1, x_2)$ is the normal displacement from this plane. In these coordinates, $\pi \circ N = \nabla w / \|\nabla w\|$, so we can compute the ramification index J_p as the degree of the map $S^1 \rightarrow S^1$ given by

$$\{(x_1, x_2) \mid x_1^2 + x_2^2 = 1\} \mapsto \frac{\nabla w(\epsilon x_1, \epsilon x_2)}{\|\nabla w(\epsilon x_1, \epsilon x_2)\|},$$

for any sufficiently small ϵ . This computation of J_p is illustrated in Fig. 6.

The winding number J_p and the order of saddleness m_p are related as shown by the following lemma:

Lemma 3.6. *Let $y : \Omega \rightarrow \mathbb{R}^3$ be a $C^{1,1}$ pseudospherical immersion, and let p be a point in Ω . Then $J_p = 1 - m_p$ where J_p is the local degree of the Gauss normal map $N : \Omega \rightarrow S^2$ at p , and m_p is the order of saddleness of the immersion y at p .*

Proof. We remark that the quantities m_p and J_p are well defined for $C^{1,1}$ immersion (and even for immersions with lower regularity), since $N : \Omega \rightarrow S^2$ is continuous (even Lipschitz) [43]. The equality $J_p = (1 - m_p)$ is known from the theory of weakly regular saddle surfaces (cf. [82, Lemma 1.2]). We will have further use for the intuition behind this result so we give a short, self contained argument that holds for branched $C^{1,1}$ surfaces. Our argument is based on the Lelievre equations (3.4).

By invariance under Euclidean motions, we can, WLOG, assume that $y(p) = 0, N(p) = \mathbf{e}_3$. A saddle of order m is defined by angles $0 = \beta_0 < \beta_1 < \dots < \beta_{2m} = 2\pi$ such that the tangent vectors, at p , to the u and v asymptotic curves are given by $\mathbf{s}_i = \cos(\beta_i)\mathbf{e}_1 + \sin(\beta_i)\mathbf{e}_2$ (cf. Eq. (3.10)).

From (3.4), we have, $N_u = N \times r_u, N_v = -N \times r_v$, so the asymptotic curves lift to S^2 by the normal map N into curves whose tangents at $N(p) = \mathbf{e}_3$ are given by $\mathbf{t}_i = \cos(\theta_i)\mathbf{e}_1 + \sin(\theta_i)\mathbf{e}_2$ where $\theta_i = \beta_i + \frac{\pi}{2} \bmod 2\pi$ if i is even and $\theta_i = \beta_i - \frac{\pi}{2} \bmod 2\pi$ if i is odd. We can determine the values of θ_i by imposing the requirement $0 < \theta_i - \theta_{i+1} < \pi$, which is necessary to ensure that $N_u \times N_v = -r_u \times r_v$. Since $0 < \beta_{i+1} - \beta_i < \pi$, it follows that $\theta_{i+2} - \theta_i = \beta_{i+2} - \beta_i - 2\pi$. Adding up the differences in the θ_i , we thus get

$$\sum_{i=1}^{2m} [\theta_i - \theta_{i-1}] = \sum_{k=1}^m [\theta_{2k} - \theta_{2k-2}] = \beta_{2m} - \beta_0 - 2m\pi = 2(1 - m)\pi,$$

thus proving the claim that $J_p = 1 - m_p$. □

Fig. 6 is an illustration of this result. It seems “obvious” that there is no “nice” way to approach the monkey saddle (Fig. 6c) through normal saddle surfaces (Fig. 6a), since we cannot go from a winding number of 1 to a winding number of 2 continuously. This is indeed the case, but the argument needs to be more refined, as we show below in Theorem 3.8. This theorem encapsulates the principal motivation for investigation of pseudospherical surfaces with branch points, namely that surfaces with branch points are distinct from smooth surfaces pseudospherical surfaces because they carry a topological index that cannot be smoothed away. Our approach is based on the ideas of Brezis and Nirenberg for the degree of BMO mappings [18, 19].

Lemma 3.7. *Let $\Omega \subset \mathbb{H}^2$ denote a (proper) open subset of the Hyperbolic plane and let $y : \Omega \rightarrow \mathbb{R}^3$ be a C^2 pseudospherical immersion. For every point $p \in \Omega$, there exist $\delta > 0$ and $d_0 > 0$ such that:*

- (1) *The normal map $N : B_{2\delta}(p) \rightarrow S^2$ satisfies $N(x) \neq N(p)$ for any x in the punctured ball $B_{2\delta}(p) \setminus \{p\}$.*

(2) For all x in the ‘collar’ $B_{2\delta}(p) \setminus \overline{B_\delta(p)}$, we have $\|N(x) - N(p)\| \geq d_0$.

This is also true for branched pseudospherical immersions, i.e. immersions built from assembling C^2 immersions by cutting and patching along asymptotic lines.

Proof. If y is a C^2 immersion, the normal map $N : \Omega \rightarrow S^2$ is an immersion at p and thus injective in a neighborhood of p , implying the existence of an appropriate $\delta > 0$ such that for all $x \in B_{3\delta}(p) \setminus \{p\}$ we have $N(x) \neq N(p)$. Since $\overline{B_{2\delta}(p)} \setminus B_\delta(p)$ is a compact subset of $B_{3\delta}(p) \setminus \{p\}$ and N is continuous, the conclusions follow.

If y is a branched immersion, the normal map is certainly not injective in any neighborhood of a branch point p . This follows from the fact that p is a ramification point for the Gauss Normal map $N : \Omega \rightarrow S^2$. However, if $S_i \subset \Omega$ is one sector at the branch point p , we can extend the asymptotic curves bounding S_i smoothly so that the extensions satisfy Eq. (3.3). As in Prop. 3.4, we can now construct a C^2 immersion \tilde{y}_i on a neighborhood of p , one that agrees with y on the sector S_i . Thus there is a $\delta_i > 0$ such that $N(x) \neq N(p)$ on $S_i \cap B_{\delta_i}(p)$. Setting $\delta = \min(\delta_0, \delta_1, \dots, \delta_{2m_p-1})$ gives a $\delta > 0$ with the required property. \square

The preceding lemma gives us control on the size of a set that we can use to compute the ‘local’ degree of the normal map at a point p . Since we will consider sequences of pseudospherical immersions y_n we will ask that this size δ be uniform for the sequence.

Theorem 3.8. *Let Ω denote an open, simply connected, domain in the Hyperbolic plane and $y : \Omega \rightarrow \mathbb{R}^3$ be a $C^{1,1}$ immersion, possibly with branch points. Assume that y is well approximated by C^2 pseudospherical immersions, i.e there exists a sequence of pseudospherical immersions $y_n : \Omega \rightarrow \mathbb{R}^3$ such that*

- (1) $y_n \rightarrow y$ in $W_{loc}^{2,2}$.
- (2) For all $p \in \Omega$, there exist $\delta(p) > 0, d_0(p) > 0$ such that, for a subsequence y_{n_k} , the conclusions of Lemma 3.7 are satisfied for all n_k , with $\delta = \delta(p)$ and $d_0 = d_0(p)$.

Then $m_p = 2$.

Proof. For the C^2 immersions, N is locally one to one [43] and $J_p^{(n)}$, the local degree of the normal map N_n at $N_n(p)$ is -1 (from the reversal of orientation). $W_{loc}^{2,2}$ convergence of the immersions y implies $W^{1,2}$ convergence of the Normal maps on compact sets (here $\overline{B_{2\delta}(p)}$). Convergence of the normals in $W^{1,2}(\overline{B_{2\delta}(p)})$ implies convergence in BMO [32, §5.8.1] as well as in $L^1(\overline{B_{2\delta}(p)})$. Our maps N_n thus satisfy the hypotheses required for the stability of degree under BMO convergence [19, Property 2, §II.2]. This implies $J_p = -1$ for the immersion y . Lemma 3.6 now implies that $m_p = 2$. \square

We expect that the second hypothesis in Theorem 3.8 is redundant, and the fact that the limiting map y has an appropriate δ, d_0 at the point p should suffice to show uniformity of these quantities for (a subsequence of) y_n . Also, this condition can be replaced by more ‘physically motivated’ hypotheses, for instance, by demanding that the immersions y_n have uniform (local) bounds for the extrinsic curvatures and the geodesic curvatures

of asymptotic lines. Analysis of the the frame equations (3.3) will then give quantitative estimates, uniform in n , for δ and d_0 . We will explore these issues elsewhere.

According to Thm. 3.8, the monkey saddle in Fig. 6c *cannot* be approximated, in $W_{\text{loc}}^{2,2}$, by sequences of C^2 pseudospherical immersions that admit a uniform choice of δ, d_0 at the location of the branch point. In physical terms, the index m_p (or equivalently J_p) makes branch points *topological defects*, and they cannot be “smoothed out” into states with nearly the same elastic (bending) energy.

Let $B_R \subset \mathbb{H}^2$ denote a geodesic ball of radius R in the Hyperbolic plane. We define the following quantities:

$$\begin{aligned} \mathcal{E}_R^2 &= \inf \{ \mathcal{E}(y) : y : B_R \rightarrow \mathbb{R}^3 \text{ is a } C^2 \text{ isometry} \}, \\ \mathcal{E}_R^{\text{bs}} &= \inf \{ \mathcal{E}(y) : y : B_R \rightarrow \mathbb{R}^3 \text{ is a piecewise } C^2 \text{ isometry with isolated branch points} \}, \\ \mathcal{E}_R^{1,1} &= \inf \{ \mathcal{E}(y) : y : B_R \rightarrow \mathbb{R}^3 \text{ is a } C^{1,1} \text{ isometry} \}. \end{aligned}$$

$\mathcal{E}_R^{\text{bs}}$ is the infimum over piecewise C^2 , globally $C^{1,1}$ isometries $y : B_R \rightarrow \mathbb{R}^3$, with isolated *branch points* where the local structure is as detailed in Prop. 3.4. By containment relations among the classes of admissible mappings, we have the ordering

$$(3.13) \quad \mathcal{E}_R^{1,1} \leq \mathcal{E}_R^{\text{bs}} \leq \mathcal{E}_R^2.$$

Theorem 3.8 allows/suggests the possibility that some of these inequalities are strict. In particular, the infimum of the $W^{2,2}$ norm, i.e. the *Willmore* or the *bending* energy of isometric immersions $y : B_R \rightarrow \mathbb{R}^3$ for $C^{1,1}$ branched isometries can be strictly smaller than the infimum over C^2 or smoother isometries, since we cannot approximate all branched isometries by smooth ones in $W^{2,2}$. The existence of an energy gap between these two regularity classes is certainly unexpected, since branched isometries can indeed be approximated by smooth mappings (but not, as we argue below, by smooth isometries). We present numerical evidence to support the existence of an energy gap (see Fig. 21a), and this is key to explaining the ubiquity of undulating morphologies for hyperbolic sheets in nature, despite the existence of “smoother” isometries [36].

Remark 3.9. Note that Thm. 3.8 does not imply that y , a $W_{\text{loc}}^{2,2}$ limit of C^2 pseudospherical immersions y_n , is necessarily C^2 , although the local degree of y is -1 everywhere. Indeed, the construction from Eq. 3.10 with $m = 2$ (4 sectors) but with $\alpha_1 + \alpha_2 \neq \pi$ and $\alpha_2 + \alpha_3 \neq \pi$ gives a piecewise smooth, non- C^2 surface in any neighborhood of p since the u and the v asymptotic curves through p (respectively γ_u and γ_v) are not differentiable at p . However, γ_u and γ_v can be uniformly approximated by smooth solutions of Eq. (3.3) by smoothing the (distributional) geodesic curvature(s) κ_u (respectively κ_v) of γ_u (resp. γ_v). Using these smoothed asymptotic curves along with the Lelievre equations, we obtain smooth pseudospherical surfaces that converge to a $C^{1,1}$ immersion with $J = -1$ everywhere.

3.3. Introducing a new branch point: Surgery. Here we outline another specific example of a branched surface, illustrating an approach that we call *surgery*, in contrast to the approach of *assembly* in the previous section. In the process of surgery, we introduce a branch point into a “pre-existing” PS-front.

Let $\Omega = [0, u_{\max}] \times [0, v_{\max}]$ be a rectangular domain in the first quadrant $u \geq 0, v \geq 0$. We start with a base PS-front $r_0 : \Omega \rightarrow \mathbb{R}^3$ that is an Amsler patch, corresponding to (3.12) with the choices $\mathbf{z} = 0, \mathbf{n} = \mathbf{e}_3, \mathbf{e}_u = \mathbf{e}_1$ and $\mathbf{e}_v = \mathbf{e}_2$. We then select an interior point (u^*, v^*) with $u^* > 0, v^* > 0$, hereafter referred to as a *branch point*. We set

$$(3.14) \quad \mathbf{z}_1 = r_0(u^*, v^*), \quad \mathbf{n}_1 = N_0(u^*, v^*), \quad \mathbf{g}_u = \partial_u r_0(u^*, v^*), \quad \mathbf{g}_v = \partial_v r_0(u^*, v^*).$$

We define the L -shaped region $\Omega^* \subset \Omega$ by $\Omega^* = \Omega \setminus [u^*, u_{\max}] \times [v^*, v_{\max}]$.

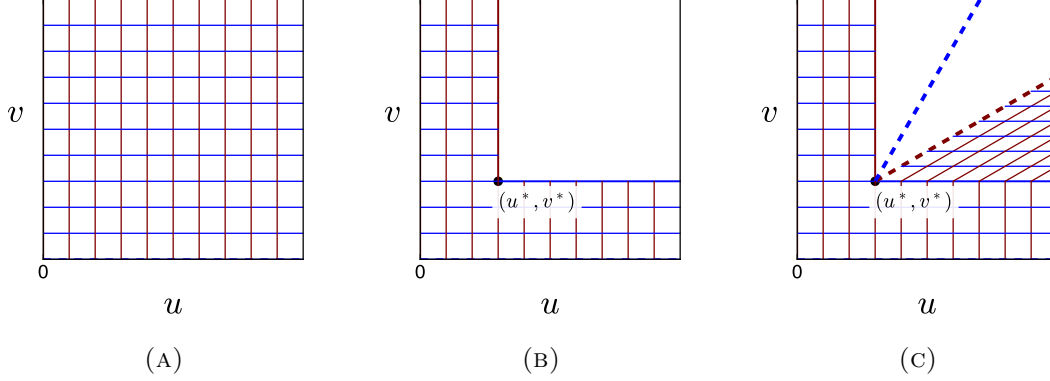


FIGURE 7. Surgery for asymptotic coordinate patches in Ω . (a) Ω , (b) Ω^* , and (c) $\Omega^* \cup \Omega_1$. The normal field along the u -line in Ω_1 is obtained by copying the corresponding data from the immersion of Ω^* .

We construct three PS-fronts r_1, r_2 and r_3 on sectors Ω_1, Ω_2 and Ω_3 respectively which are then assembled with the PS-front r_0 on Ω^* as in §3.2. The procedure for gluing the patches is outlined in Figure 7, and the corresponding gluing procedure for the immersions, r_i is illustrated in Figure 8.

We will take r_2 to be an Amsler patch on Ω_2 with boundary conditions given by (3.12) with data inherited from r_0 through (3.14). Specifically, we set

$$(3.15) \quad \mathbf{z} = \mathbf{z}_1, \quad \mathbf{n} = \mathbf{n}_1, \quad \mathbf{e}_u^{(1)} = \frac{2\mathbf{g}_v + \mathbf{g}_u}{\|2\mathbf{g}_v + \mathbf{g}_u\|}, \quad \mathbf{e}_v^{(1)} = \frac{2\mathbf{g}_u + \mathbf{g}_v}{\|2\mathbf{g}_u + \mathbf{g}_v\|},$$

as an approximation to trisecting the angle between the asymptotic curves at the branch point. Solving (3.8) and (3.4) gives N_2 and the corresponding PS-front r_2 .

To build the Gauss map, $N_1 : \Omega_1 \rightarrow S^2$, again, we need only prescribe normal data along the axes: $u \geq 0$ and $v \geq 0$, where the coordinates (u, v) are now “local” to Ω_1 . We get data along $v = 0$ by copying it from the normal field N_0 :

$$(3.16) \quad N_1(u, 0) = N_0(u - u^*, v^*) \text{ for } u \in [0, u_{\max} - u^*],$$

The data for N_1 along $u = 0$ comes from the PS-front r_2 :

$$(3.17) \quad N_1(0, v) = N_2(0, v) = \cos(v)\mathbf{n}_1 - \sin(v)\mathbf{n}_1 \times \mathbf{e}_v^{(1)}.$$

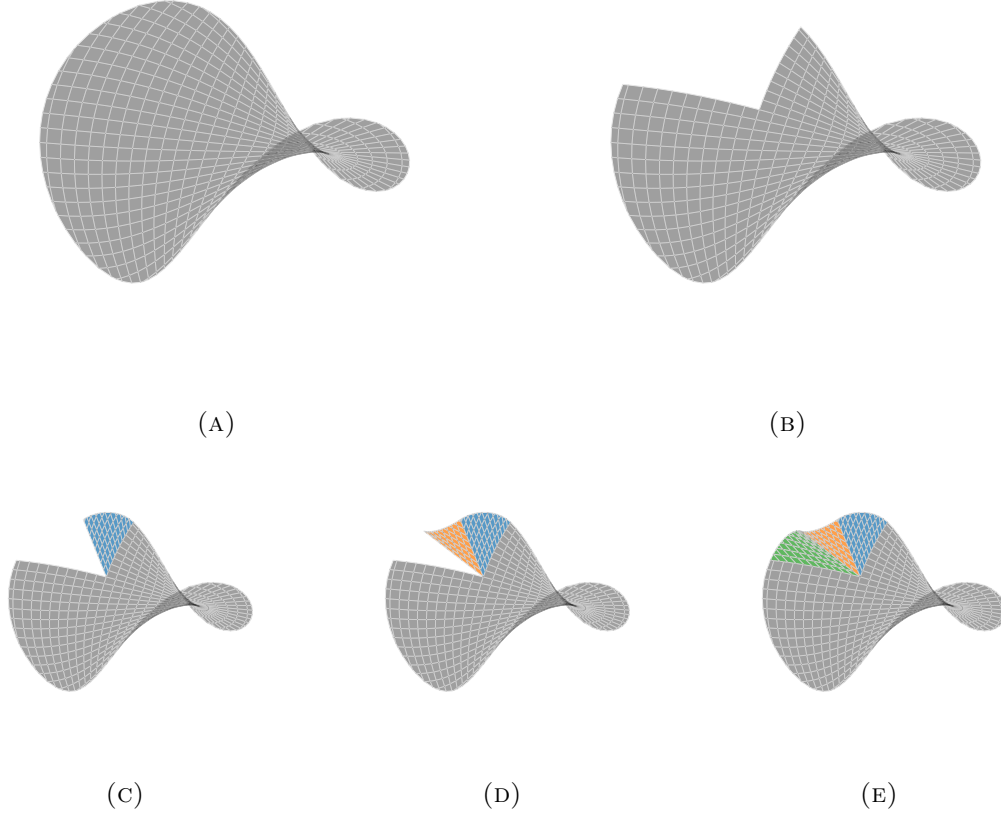


FIGURE 8. Introducing a branch point into a smooth hyperbolic surface away from the origin. The resulting sectors have curved edges.

We can now obtain a weakly harmonic normal field N_1 by solving the Moutard equation (3.8) on the rectangle Ω_1 and then integrating the Lelievre equations to obtain the PS-front r_1 . Similarly, we obtain r_3 on Ω_3 from the data

$$N_3(0, v) = N_0(u^*, v - v^*) \text{ for } v \in [0, v_{\max} - v^*]$$

$$N_3(u, 0) = N_2(u, 0) = \cos(u) \mathbf{n}_1 + \sin(u) \mathbf{n}_1 \times \mathbf{e}_u^{(1)}.$$

As in the previous section, we can assemble the PS-fronts r_0, r_1, r_2 and r_3 and (if needed) pick a subdomain such where $N_u \times N_v$ does not vanish, to obtain a $C^{1,1}$ isometric immersion with $K = -1$. The topological structure of the asymptotic lines corresponds to a monkey saddle ($2m = 6$) at the branch point (u^*, v^*) – there are six asymptotic rays extending from the branch point. Otherwise, there exist exactly four asymptotic directions extending from every other point.

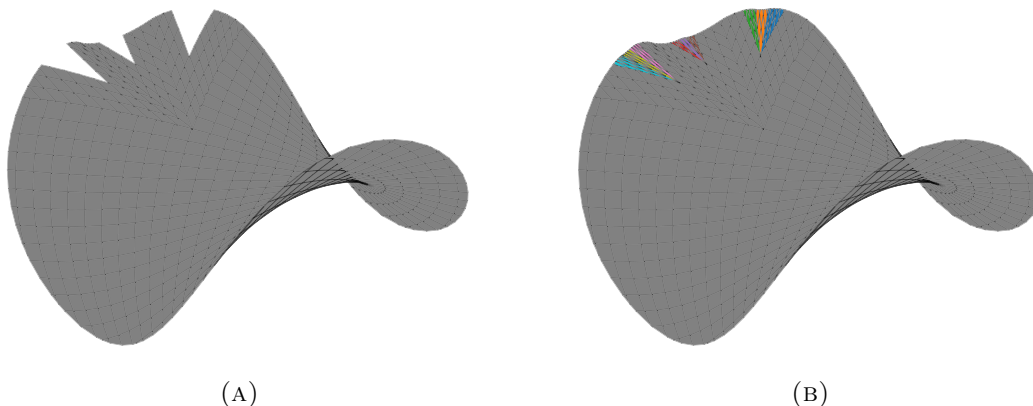


FIGURE 9. Recursively performing surgery on an initially smooth surface.

It is clear how we can repeat this procedure recursively by picking branch point, cutting out one sector from this branch point, and replacing it with 3 new sectors. We call this procedure *surgery* to contrast it with the procedure in §3.2, which we refer to as *assembly*. Surfaces with a second generation of branch points are shown in Figure 9.

3.4. The asymptotic skeleton. As we discussed above in §3.2 and §3.3, our surfaces are combinatorial objects built by gluing together multiple copies of a basic template, an *asymptotic quadrilateral* (see Definition 3.3). The combinatorial structure of such a surfaces, that reflects the different ways in which asymptotic quadrilaterals can be glued together, is encoded in a structure we call its *asymptotic skeleton*.

To define these objects we first recall the notion of (piecewise linear) measured foliations of subsets of \mathbb{R}^2 . We follow the discussion in Thurston [91] and Fathi, Laudenbach and Poénaru [33] and adapt it to our situation. Interestingly, measured foliations are also the appropriate mathematical structures for describing the topology of defects in smectic liquid crystals [78].

Definition 3.10. D is an open subset of \mathbb{R}^2 and thus inherits a piecewise linear structure. A foliation \mathcal{F} of D is a *piecewise linear measured foliation* if every regular point of the foliation has neighborhoods U_i equipped with piecewise linear charts, i.e. homeomorphisms $g_i : U_i \rightarrow V_i \subset \mathbb{R}^2$ such that every leaf in \mathcal{F} is the inverse image of a horizontal line $x_2 = \text{constant}$. On the overlap of two such neighborhoods U_i and U_j , the transition functions $g_i \circ g_j^{-1} : g_j(U_i \cap U_j) \rightarrow \mathbb{R}^2$ is of the form $(x_1, x_2) \mapsto (f_{ij}(x_1, x_2), c_{ij} \pm x_2)$ where f_{ij} is piecewise linear and c_{ij} is a real constant.

We allow for the possibility of singular points, that do not have neighborhoods with this property, but require that such singular points be isolated. Examples of such piecewise linear measured foliations on (subsets of) \mathbb{R}^2 are shown in Fig. 10. For our purposes, such foliations ought to represent the u - (or v -) asymptotic curves in branched pseudospherical fronts. To properly capture the properties of asymptotic curves, namely that they cannot

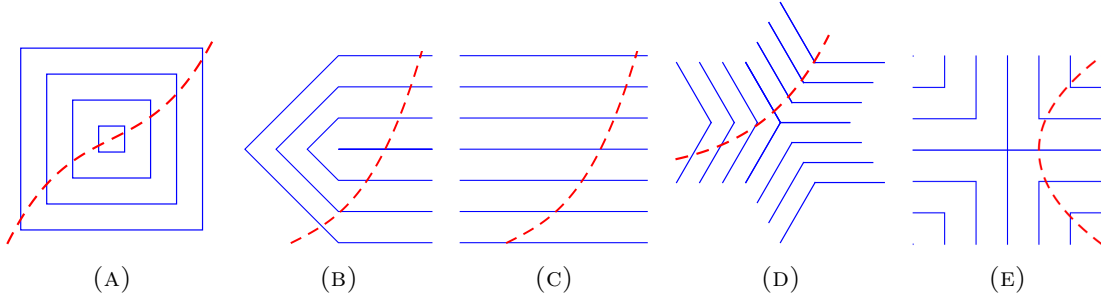


FIGURE 10. Piecewise linear measured foliations. The foliation in (C) is non-singular, and the rest have a singular point. In each case the dashed curve is transverse to the leaves in the foliation.

form loops, they come in two families with opposite senses of torsion, and they intersect transversally, we need to impose an additional conditions on the foliations. In particular, no leaf can contain a loop, and every curve γ that intersects the leaves transversally can intersect each leaf (regular or singular) only once. These conditions are not satisfied by the foliations in Figs. 10a and 10b. Consequently these foliations cannot describe the local structure of of the u - (or v -) asymptotic curves near a singular point [94]. The foliations in Figs. 10d and 10e, however, are appropriate for representing the asymptotic network near a singular point and they correspond to saddles with $m = 3$ and $m = 4$ respectively.

The requirement that curves transverse to the leaves intersect each leaf no more than once guarantees that there is a well defined notion of *separation* $|x_2 - x'_2|$ between two leaves in a foliation \mathcal{F} which is obtained by adding up the differences in the x_2 values in the coordinate charts along any curve that is transverse to the foliation [91]. This is indeed the v coordinate if defined relative to the foliation corresponding to the u - asymptotic lines. The ambiguity in the sign implies that both v and $-v$ are perfectly good coordinates for the same foliation \mathcal{F}^u , and indeed, accounting for this ambiguity is a key point in our analysis.

Definition 3.11. An (admissible) *asymptotic network* is a set $D \subseteq \mathbb{R}^2$ along with two piecewise linear measured foliations \mathcal{F}^u and \mathcal{F}^v that are *transverse*, i.e every regular point for \mathcal{F}^u is also a regular point for \mathcal{F}^v and at these regular points, the leaves intersect transversally.

Fig. 11 shows a prototypical example of an admissible asymptotic network. Note that, if \mathcal{F}^u and \mathcal{F}^v are transverse to each other, it follows from computing the Poincaré index of the vector fields normal to the leaves of \mathcal{F}^u and \mathcal{F}^v that these indices have to be equal at every point [94, §3.3]. A singular point for \mathcal{F}^u is therefore necessarily a singular point for \mathcal{F}^v with the same index and vice versa. For the foliations in Fig. 12, this common index is $-\frac{1}{2}$ and the singular points are indeed at the same location. These connections between a pair of transverse (singular) foliations, their branch points, and solutions of Hyperbolic Monge-Ampere equations were also explored by Kirchheim [58, Chap. 2].

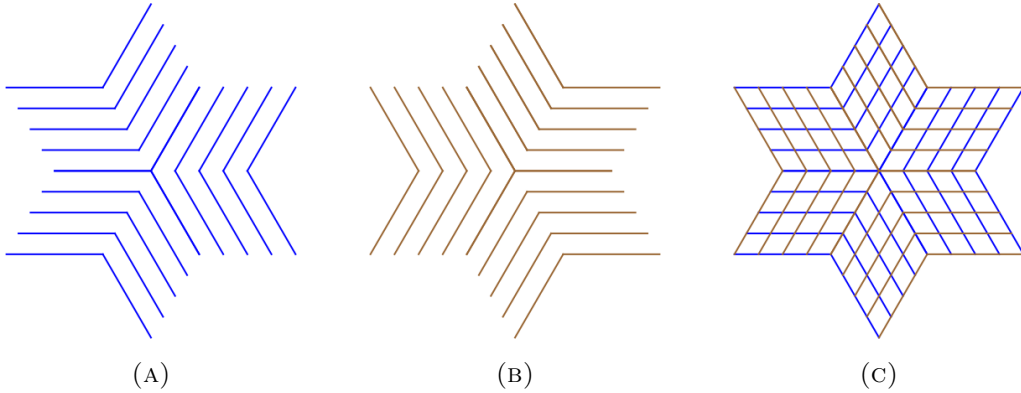


FIGURE 11. (A) A piecewise linear measured foliation \mathcal{F}^u that has a singular point with 3 branches (Poincaré index $-\frac{1}{2}$). (B) A transverse foliation \mathcal{F}^v . Note that it has the same singular point, and with the same index as \mathcal{F}^u . (C) A geometric realization of an asymptotic network $(D, \mathcal{F}^u, \mathcal{F}^v)$ in \mathbb{R}^2 . For this particular embedding, \bar{D} , the closure of the domain D , is a 6 pointed star.

Definition 3.12. An *asymptotic skeleton* is a set $S \subset D$ obtained as a union of (finitely many) leaves of the foliations $\mathcal{F}^u, \mathcal{F}^v$ with the following properties:

- (1) If L is a singular leaves in either \mathcal{F}^u or \mathcal{F}^v , then $L \subseteq S$.
- (2) Every leaf (possibly singular) in \mathcal{F}^u intersects one or more leaves in \mathcal{F}^v that are contained in S and vice versa.

From definition 3.10, it is clear that the complement of any single leaf is an open, dense subset of D . Since S contains only finitely many leaves, and it contains all the singular leaves, it follows that $D \setminus S$ consists entirely of regular points. By small local deformations, if needed, we can assume that the boundary ∂D avoids all the singular points, only intersects the singular leaves transversally, and is given by a piecewise curve with “edges” that alternate between being contained within one of the leaves in \mathcal{F}^u and one of the leaves in \mathcal{F}^v , as illustrated in Fig. 11c. (See [94, §3.4] for a discussion of why we can always do this.) It follows that $D \setminus S$ is therefore a union of (topological) 2-cubes C_i that are equipped with a canonical parametrization $\varphi_i : C_i \rightarrow (0, 1)^2$, where the leaves of \mathcal{F}^u within C_i are given by $\varphi_i^{-1}((0, 1) \times \{v_0\})$ and the leaves of \mathcal{F}^v are given by $\varphi_i^{-1}(\{v_0\} \times (0, 1))$.

The cubes C_i naturally give a cellular decomposition of D [45, 54] determined by the 2 dimensional complex $X_0 \subset X_1 \subset X_2$ (denoting the vertices, edges and faces respectively), where the 0-skeleton X_0 contains all the singular points for the foliations \mathcal{F}^u and \mathcal{F}^v , and the 1-skeleton X_1 is an asymptotic skeleton for $(D, \mathcal{F}^u, \mathcal{F}^v)$. This cellular decomposition of D is a quad-graph [14, 16] since all the faces are quadrilaterals. Furthermore, there is a globally consistent assignment of the edges, i.e. elements of X_1 , to u - and v - edges that alternate going around any vertex. This implies that every cycle in the dual graph, which crosses equal numbers of u and v edges in X_1 is even, and thus the dual graph is bipartite

[6]. In particular, this implies that the complex is checkerboard colorable as illustrated in the examples in Fig. 12. The two grids are equivalent as graphs, although the grid in Fig. 12a is naturally interpreted as the skeleton for the surface obtained by assembly in §3.2 while the grid in Fig. 12b is naturally interpreted as the result of surgery by excising a quadrant and replacing by 3 sectors, as in §3.3.

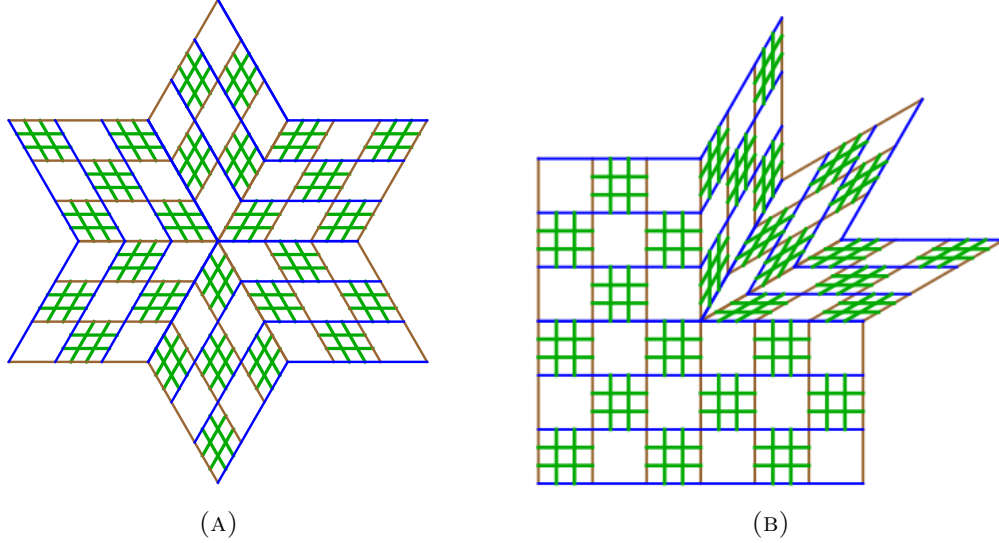


FIGURE 12. Examples of asymptotic skeleta that are embedded in the plane. The u and v edges are colored red and blue, and the checkerboard pattern is indicated by the shading.

3.5. The Sine-Gordon equation for surfaces with branch points. On a domain where the asymptotic curves and the angle function $\varphi(u, v)$ are differentiable, we can define a one form $\alpha = \frac{1}{2}(\varphi_v dv - \varphi_u du)$ and an area 2-form $\sqrt{\det(\mathbf{g})} = \sqrt{\det(g_{ij})} du \wedge dv$ where $\mathbf{g} = du^2 + 2\sigma \cos \varphi du dv + dv^2$ and the sign of the square root is picked so that the orientation induced by $\sqrt{\det(\mathbf{g})}$ agrees with the orientation induced by ω (or equivalently, by N_ω). It is now straightforward to check that $\beta = \sigma \sin \varphi du \wedge dv$. On a domain where σ does not change sign, the sine-Gordon equation (3.9) is equivalent to $d\alpha - \beta = 0$. Integrating over an asymptotic quadrilateral $R = \{u_0 \leq u \leq u_1, v_0 \leq v \leq v_1\}$ we obtain the Hazzidakis formula

$$(3.18) \quad \Delta_R \varphi \equiv \varphi(u_0, v_0) - \varphi(u_0, v_1) + \varphi(u_1, v_1) - \varphi(u_1, v_0) = A(R)$$

where $\Delta_R \varphi = \sum (-1)^{\ell_i} \varphi_i$, i indexes the vertices in the quadrilateral, ℓ_i is the modulo 2 length of any path from the vertex (u_0, v_0) to the vertex labelled i , and A is the area of (the immersion of) the quadrilateral. In order that R be immersed into \mathbb{R}^3 , we must have $0 < \varphi(u, v) < \pi$ on R , which gives $A(R) < 2\pi$ for any immersed asymptotic quadrilateral. The Hazzidakis formula (3.18) holds even in circumstances where φ is not differentiable.

For C^{1M} PS-fronts φ only needs to be C^0 but this formula still holds and the sine-Gordon equation can be interpreted in a distributional sense [25].

Eq. (3.18) naturally extends to domains Γ that are bounded by a piecewise C^1 Jordan curve $\gamma = \partial\Gamma$ consisting of arcs that are either u or v asymptotic curves, i.e. leaves in \mathcal{F}^u or \mathcal{F}^v . Since two curves from the same family can not intersect, the arcs alternate between the u and the v curves. Such curves γ are examples of *Hamburger polygons* [94]. Integrating the sine-Gordon equation $d\alpha - \beta = 0$ on Γ , we get

$$(3.19) \quad \Delta_\Gamma \varphi \equiv \sum_i (-1)^{\ell_i} \varphi_i = \oint_\gamma \alpha = \int_\Gamma \beta = A(\Gamma),$$

where i indexes the vertices in the Hamburger polygon and ℓ_i is $0 \bmod 2$ at every initial vertex for an arc from the u -family (also a terminal vertex for a v -arc) and $\ell_i = 1 \bmod 2$ at every terminal vertex of a u -arc (resp. initial vertex of a v -arc), with respect to the orientation on γ that is induced by ω .

We will now generalize this result to $C^{1,1}$ branched pseudospherical surfaces. For C^{1M} surfaces, with a continuous φ , we see that $\Delta_\Gamma \equiv \Delta(\Gamma) \rightarrow 0$ as $A(\Gamma) \rightarrow 0$, so there is no *concentration* for the quantity $\Delta_\Gamma = \oint_{\partial\Gamma} \alpha$ on sets of vanishing area. For our branched surfaces, φ is not always continuous. φ necessarily has jumps across the asymptotic curves that are incident on a branch point. This might potentially result in concentration of Δ on these ‘‘singular’’ objects. We can determine the potential concentrations of Δ on branch points, and along the asymptotic curves that are incident on branch points, by using appropriate Hamburger polygons as illustrated in Fig. 13.

For the ε -thin ‘‘rectangle’’ R_ε shown in Figure 13a, we have $\Delta_{R_\varepsilon} = \varphi(r_\varepsilon^+) - \varphi(r_\varepsilon^-) + \varphi(q_\varepsilon^-) - \varphi(q_\varepsilon^+)$. Let us first assume that this rectangle straddles a singular leaf in \mathcal{F}^u . In this case, we can estimate $\varphi(r_\varepsilon^+) - \varphi(q_\varepsilon^+) = \int \partial_u \varphi^+ du + O(\varepsilon)$ noting that the integral is taken entirely on one side of the singular leaf, so there are no discontinuities along the integration path. Similarly, $\varphi(r_\varepsilon^-) - \varphi(q_\varepsilon^-) = \int \partial_u \varphi^- du + O(\varepsilon)$. Although φ^+ and φ^- , the limits of the angle φ between the characteristic curves from either side of the singular leaf are different, their derivatives $\partial_u \varphi^\pm = -\kappa^u$ have to match, since they are both equal to the geodesic curvature of a curve that is common to both sectors (See Eq. (3.9)). Consequently, $\Delta_{R_\varepsilon} = O(\varepsilon)$. A similar argument also applies to singular leaves in \mathcal{F}^v . Thus, there is no concentration of Δ along the asymptotic curves that are incident on branch points.

We now consider the concentration of Δ on branch points. Let p be a branch point with order of saddleness m_p enclosed by a $2m_p$ pointed, ε -small, star T_ε , comprising of asymptotic rhombii $R_0, R_1, \dots, R_{2m_p-1}$ as shown in Figure 13a. As discussed in Prop. 3.4, the local structure is given by alternating sets of m_p u -curves and m_p v -curves that are incident at p with well defined tangent directions.

Let $\alpha_i, i = 0, 1, 2, \dots, 2m_p - 1$ denote the angle of the rhombus R_i at p with respect to the orientation ω induced by the normal $N(p)$. This is consistent with the definitions in §3.2. Clearly $\sum_{i=0}^{2m_p-1} \alpha_i = 2\pi$. From Eq. (3.6), we see that the angles between the asymptotic directions at p are given by comparing the sense of the rotation from r_u to r_v ,

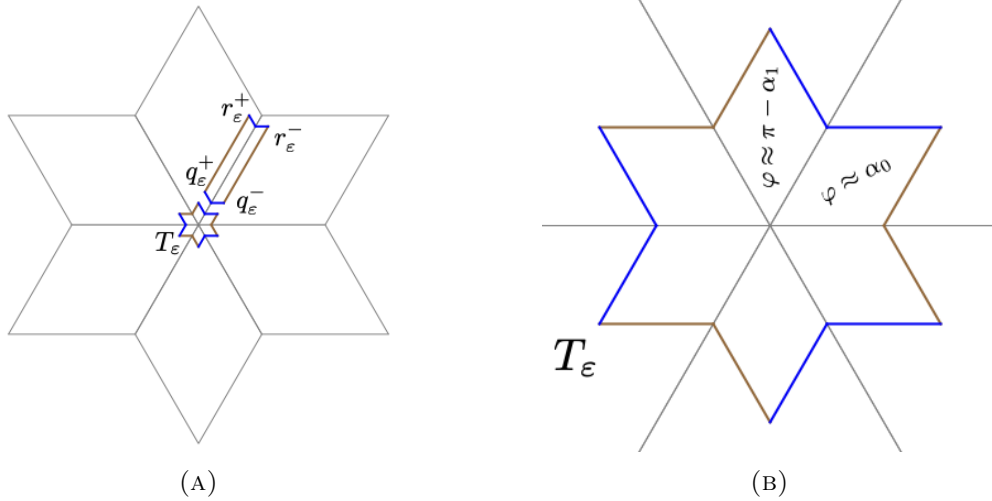


FIGURE 13. (a) The Hamburger polygon T_ϵ allows us to compute the concentration of Δ at the central branch points and the rectangle $R_\epsilon = [q_\epsilon^- r_\epsilon^- r_\epsilon^+ q_\epsilon^+]$ determines the concentration on an asymptotic curve incident on the branch point. (b) Blowing up the polygon T_ϵ . The angle φ is nearly constant on each sector. $\varphi = \alpha_{2i}$ on the even sectors and $\varphi = \pi - \alpha_{2i+1}$ on the odd sectors, where α_j is the angle between the asymptotic curves bounding the j^{th} sector.

chosen to be directed away from p , with the orientation induced by ω :

$$(3.20) \quad \varphi_i = \begin{cases} \alpha_i & \text{if } r_u \text{ to } r_v \text{ is counter-clockwise} \\ \pi - \alpha_i & \text{otherwise} \end{cases}$$

On each rhombus R_i , the surface restricts to a C^2 (even smooth) PS-front, so it follows that φ is continuous. In particular, at the vertex q_i , diagonally across from p in R_i , we have $\varphi(q_i) = \varphi_i + O(\epsilon)$. We can now compute,

$$(3.21) \quad \Delta_{T_\epsilon} = \sum_i (-1)^i \varphi_i + O(\epsilon) = -(m_p - 2)\pi + O(\epsilon)$$

This calculation shows that branch points do indeed concentrate Δ . This concentration has a definite sign, and it is zero at points where the surface is locally a 2-saddle, as we would expect. This again underscores the importance of the order of saddleness m_p (or equivalently the ramification index $J_p = 1 - m_p$) as an important topological invariant. It encapsulates key properties of branched PS-fronts. It also precludes the possibility of approximating branched PS-fronts by smooth hyperbolic surfaces. It is a quantitative signature of how wrinkled hyperbolic surfaces (“lettuce”) are distinct from their regular-saddle counterparts.

It is straightforward to “globalize” the arguments from above to get a generalization of the (integrated form) of the sine-Gordon equation that is valid even for $C^{1,1}$ branched pseudospherical immersions. We record this in the following theorem:

Theorem 3.13. $r : (\Omega, g) \rightarrow \mathbb{R}^3$ is a branched pseudospherical immersion, i.e. a piecewise C^2 , globally $C^{1,1}$ immersion with finitely many isolated branch points $p_i, i = 1, 2, \dots, k$, where the local structure corresponds to a saddle of order $m_i \geq 3$.

ω is an orientation on Ω . $\Gamma \subset \Omega$ is a domain with compact closure in Ω whose boundary $\gamma = \partial\Gamma$ is a Hamburger polygon with vertices $q_0, q_1, \dots, q_{2j-1}$. The vertices are indexed so that q_{2n} is an initial vertex for a u -arc and q_{2n+1} is an initial vertex for a v -arc, with respect to the orientation ω .

The angle φ between the asymptotic curves is defined by $\sigma = \text{sign}(\omega(\partial_u r, \partial_v r))$, $\sin \varphi = \|\partial_u r \times \partial_v r\|$, $\cos \varphi = \sigma \partial_u r \cdot \partial_v r$. Then, we have

$$(3.22) \quad \Delta_\Gamma \equiv \sum_{n=0}^{2j-1} (-1)^n \varphi(q_n) = A(\Gamma) - \sum_{p_i \in \Gamma} (m_i - 2)\pi$$

Remark 3.14. The principal curvatures of a pseudospherical immersion are given by $\kappa_1 = \tan \frac{\varphi}{2}$, $\kappa_2 = -\cot \frac{\varphi}{2}$ so $\kappa_1 \kappa_2 = -1$. The Willmore energy is given by a density $\kappa_1^2 + \kappa_2^2$, and the $W^{2,\infty}$ energy is given by $\sup_{x \in \Omega} \max(|\kappa_1(x)|, |\kappa_2(x)|)$. In either case, optimizing the energy demands that we keep $\varphi \approx \frac{\pi}{2}$ everywhere, and certainly away from $\varphi = 0$ or π , i.e. we avoid the singular edge.

If φ were identically equal to $\frac{\pi}{2}$, the left hand side of (3.22) is zero since there are equal number of positive and negative contributions from $\varphi(q_n)$. The right hand side, however, is a difference between two positive quantities, the continuously varying quantity $A(\Gamma)$ and a discrete quantity $\sum_{p_i \in \Gamma} (m_i - 2)\pi$. It is therefore impossible to have $\varphi \equiv \frac{\pi}{2}$ everywhere. This also suggests the need to distribute branch points on Ω so there is “quasi-local” cancellation between the area form and the the branch point contributions, i.e energy optimal branched pseudospherical immersions will arise from attempting to place, on average, 1 branch point with $m = 3$ in every Hamburger polygon Γ with area $A(\Gamma) = \pi$. Each such branch point adds an extra undulation to the surface, that persists from the branch point out to the boundary.

4. DISCRETE DIFFERENTIAL GEOMETRY FOR BRANCHED HYPERBOLIC SURFACES

Our goal is to construct discrete analogs of the geometric notions in §3. Our approach is to discretize the asymptotic network of a $C^{1,1}$ saddle surface and obtain a graph Q^ϵ , to be used in conjunction with the Lelievre formulae, to construct discrete approximations to $C^{1,1}$ branched hyperbolic surface. We saw above that branched surfaces are realized as (subsets of) patched asymptotic rectangles, with the combinatorics given by the asymptotic skeleton, a quadgraph.

The appropriate discretization of each asymptotic rectangle is through a rectangular subset $\{i_1, i_1+1, i_1+2, \dots, i_2\} \times \{j_1, j_1+1, j_1+2, \dots, j_2\} \subset \mathbb{Z}^2$. The sets $\{(i, j_0) \mid i_1 \leq i \leq i_2\}$ and $\{(i_0, j) \mid j_1 \leq j \leq j_2\}$ are the discrete leaves from the foliations \mathcal{F}^u , respectively \mathcal{F}^v .

On every u edges where adjacent asymptotic rectangles (i, j_0) and (i', j'_0) overlap, we have $i' = k_0 + ci$ where k_0 and the sign $c = \pm 1$ are the same for all the nodes on the edge. The resulting structure is determined by the asymptotic network $(D, \mathcal{F}^u, \mathcal{F}^v)$ and can be realized by refining the asymptotic skeleton S to obtain a quadgraph $Q^\epsilon \supseteq S$. As with the ‘continuous’ construction in §3, we will first construct a discrete Lorentz-harmonic normal field $N^\epsilon : Q^\epsilon \rightarrow S^2$, and then determine the corresponding discrete immersion $r^\epsilon : Q^\epsilon \rightarrow \mathbb{R}^3$ using an appropriate discretization of the Lelievre equations (3.4).

Within each face of the asymptotic skeleton, generating a PS-front reduces to solving (3.8). As we discussed above the discretization uses square grids, i.e. subsets of \mathbb{Z}^2 , so we denote an arbitrary node by (i, j) . The Gauss map takes this grid to a discrete Chebyshev net on S^2 , i.e. a collection of geodesic parallelograms [84, 98]. We use the following notation, which is standard in DDG [15], to denote the discretization of a function f on an elementary quad:

$$(4.1) \quad f_{i,j} = f_0, f_{i+1,j} = f_1, f_{i,j+1} = f_2, \text{ and } f_{i+1,j+1} = f_{12}.$$

The following discretization for pseudospherical surfaces goes back to the work of Sauer [84] and Wunderlich [98]. The discretization of the condition that the normal field is Lorentz harmonic, Eq. (3.5), is given by

$$(4.2) \quad \begin{aligned} N_{uv} \times N &\mapsto (N_{12} + N_0 - (N_1 + N_2)) \times \frac{(N_0 + N_1 + N_2 + N_{12})}{4} \\ &= \frac{2}{4} (N_0 \times N_1 - N_1 \times N_{12} + N_{12} \times N_2 - N_2 \times N_0) \\ &= \frac{1}{2} (N_0 + N_{12}) \times (N_1 + N_2) \end{aligned}$$

The Lelievre formulae (3.4) are discretized as

$$(4.3) \quad \begin{aligned} r_u &\mapsto r_{i+1,j} - r_{i,j} \\ r_v &\mapsto r_{i,j+1} - r_{i,j} \\ N_u \times N &\mapsto (N_{i+1,i} - N_{i,j}) \times N_{i,j} = N_{i+1,j} \times N_{i,j} \\ N_v \times N &\mapsto N_{i,j+1} \times N_{i,j}. \end{aligned}$$

The discrete Lelievre equations can therefore be recast as

$$(4.4) \quad \begin{aligned} r_{i+1,j} &= r_{i,j} + N_{i+1,j} \times N_{i,j} \\ r_{i,j+1} &= r_{i,j} - N_{i,j+1} \times N_{i,j} \end{aligned}$$

Consequently, on a single quad we have two possible definitions of r_{12} , either from the path $0 \rightarrow 1 \rightarrow 12$ or the path $0 \rightarrow 2 \rightarrow 12$. Compatibility requires that we get the same answer either way, i.e.

$$(4.5) \quad N_1 \times N_0 - N_{12} \times N_1 - (-N_2 \times N_0 + N_{12} \times N_2) = (N_1 + N_2) \times (N_0 + N_{12}) = 0$$

This is precisely the same equation as (4.2). This discretization therefore has the remarkable property that the discretization of the (continuous) compatibility condition for the Lelievre formulae is *exactly* the same as the discrete compatibility of the discrete

Lelievre formulae, rather than, as one might plausibly imagine, a numerical approximation that recovers the exact result in the limit the discretization size h goes to zero. This particular discretization exemplifies a key idea in discrete differential geometry (DDG) [15, 17]. Rather than serving merely as numerical discretizations of the “true” (continuous) differential geometry, DDG is a complete theory in its own right [15].

Now we exhibit the solution for a discrete Goursat problem, namely specifying $N(i, 0)$ and $N(0, j)$ and solving for $N(i, j)$, on a single quad element. Consider a (u, v) -coordinate square indexed using subscripts $(0, 1, 2, 12)$ as before. Assume that N_{12} is unknown, while values for N_0, N_1 and N_2 are known. Then (4.2) requires

$$N_{12} = \nu(N_1 + N_2) - N_0,$$

for some $\nu \in \mathbb{R}$, as is the case for a Moutard net [17]. The condition that N_{12} is a unit vector gives a quadratic equation for ν :

$$\begin{aligned} \langle N_{12}, N_{12} \rangle &= \nu^2 \langle N_1 + N_2, N_1 + N_2 \rangle - 2\nu \langle N_1 + N_2, N_0 \rangle + \langle N_0, N_0 \rangle \\ &= \nu^2 \|N_1 + N_2\|^2 - 2\nu \langle N_1 + N_2, N_0 \rangle + 1, \end{aligned}$$

which reduces to

$$0 = \nu (\nu \|N_1 + N_2\|^2 - 2 \langle N_1 + N_2, N_0 \rangle).$$

This implies that $\nu = 0$ and $N_{12} = -N_0$ or $\nu = 2 \frac{\langle N_1 + N_2, N_0 \rangle}{\langle N_1 + N_2, N_1 + N_2 \rangle}$ and

$$(4.6) \quad N_{12} = \left[\frac{(N_1 + N_2)(N_1 + N_2)^T}{\langle N_1 + N_2, N_1 + N_2 \rangle} - \mathbb{I} \right] N_0.$$

The former being the antipodal point, and the latter being the desired solution. This is precisely the Householder reflection of N_0 through the plane generated by N_1 and N_2 . Though we specifically solved for $N_{12} = N_{i+1, j+1}$ above, this approach can be used to solve for any fourth normal vector provided the normal is specified at the three other corners of an element (See Figure 14a).

In the particular case $\langle N_0, N_1 \rangle = \langle N_0, N_2 \rangle = \cos \delta$, we have

$$\begin{aligned} 0 &= \langle N_{12} - N_0, N_{12} + N_0 \rangle = \nu (\langle N_{12}, N_1 + N_2 \rangle - 2 \cos \delta) \\ 0 &= \nu \langle N_1 + N_2, N_1 - N_2 \rangle = \nu \langle N_{12}, N_1 - N_2 \rangle \\ \implies \cos \delta &= \langle N_{12}, N_1 \rangle = \langle N_{12}, N_2 \rangle \\ (4.7) \quad \text{and } \sin \delta &= \|N_1 \times N_0\| = \|N_2 \times N_0\| = \|N_{12} \times N_2\| = \|N_{12} \times N_1\| \end{aligned}$$

Recursively applying (4.6) we can solve for the normal field on an asymptotic quadrilateral if it is specified on two of its boundaries, as illustrated in Fig. 14b. In addition, this procedure also determines the normal field on the other two boundaries. By the Beltrami-Enneper theorem (*cf.* (3.3) for $\partial_u N$ and $\partial_v N$), we can, WLOG, discretize these boundaries so that $\langle N_{i,0}, N_{i+1,0} \rangle = \langle N_{0,j}, N_{0,j+1} \rangle = \cos \delta$. By (4.7), we get $\langle N_{i,j}, N_{i+1,j} \rangle = \langle N_{i,j}, N_{i,j+1} \rangle = \cos \delta$ and $\|r_{i+1,j} - r_{i,j}\| = \|r_{i,j+1} - r_{i,j}\| = \sin \delta$ for all i, j , so the discrete surface r_{ij} is a discrete Chebyshev net in \mathbb{R}^3 and the corresponding normal field N_{ij} is a discrete Chebyshev net in S^2 as illustrated in Fig. 14a.

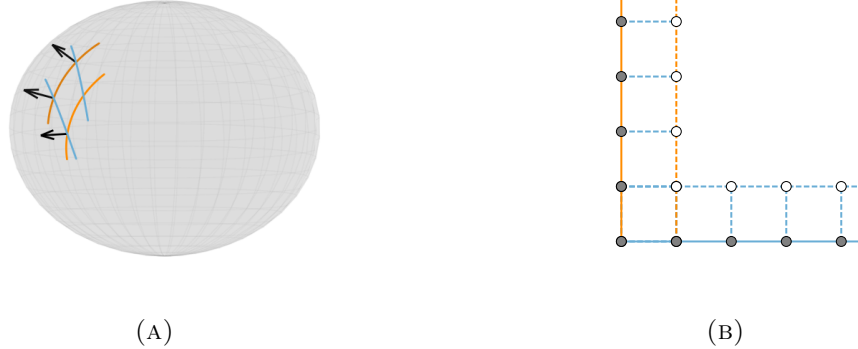


FIGURE 14. (a) A single quadrilateral in the induced Chebyshev net on S^2 . Given the normal vectors at three vertices, the normal at the fourth vertex is determined. (b) The Goursat-type discretized problem on the asymptotic quadrilateral, Ω . The nodes filled with grey represent provided boundary data, and open nodes are iteratively solved for via the system (4.2)

Our branched surfaces are obtained by patching together asymptotic quadrilaterals. We can match (the discretizations) of r and N at the boundaries (overlaps) between two adjoining asymptotic quadrilaterals by requiring that all of the spherical quadrilaterals in the (discrete) Gauss map N_{ij} are “spherical rhombii” with the same side-lengths δ , and the discrete surface (in \mathbb{R}^3) is entirely composed of “skew” rhombii with side lengths $\sin \delta$.

Given the combinatorial structure of a branched pseudospherical surface, or equivalently its asymptotic skeleton as a checkerboard colorable cellular decomposition $D = \bigcup C_i$ where each C_i is a rectangle, we can extend the recursion for solving on a single quad to the entire surface as in Proposition 3.4.

We conclude this section with some pertinent remarks:

Remark 4.1. We are given an underlying checkerboard-colorable quadmesh Q^ϵ as a discrete representation of our asymptotic network $(D, \mathcal{F}^u, \mathcal{F}^v)$. We seek a (discrete) pseudospherical immersion $r : Q^\epsilon \rightarrow \mathbb{R}^3$. We want to construct r through the discrete Lelievre formulae (4.4), which are separate equations for $\delta_u r$ and $\delta_v r$, the finite differences of r in the u and v directions. Compatibility of these equations gives the constraint (4.5) and as we discuss above, this allows us to construct a (discrete) normal field $N : Q^\epsilon \rightarrow S^2$ satisfying this constraint.

However, this is only a necessary condition for determining r , and we need a discrete Poincaré lemma to guarantee that “local” compatibility of the Lelievre equations allows us to construct a global map $r : Q^\epsilon \rightarrow \mathbb{R}^3$. This is a question about the homology of D , or equivalently the homology of the complex Q^ϵ [54]. The obstruction to constructing a global (discrete) map r is the first Homology group $H_1(Q^\epsilon)$. If D is simply connected, then every loop in D is contractible, and in this case we can always construct a global map $r : Q^\epsilon \rightarrow \mathbb{R}^3$ from the normal field $N : Q^\epsilon \rightarrow \mathbb{R}^3$.

The discrete map $r : Q^\epsilon \rightarrow \mathbb{R}^3$ is an A -net [17, 51], and the edges of the quads in Q^ϵ map to approximations of the asymptotic curves of the underlying surface.

Remark 4.2. We henceforth consider the discrete mappings $N : Q^\epsilon \rightarrow S^2, r : Q^\epsilon \rightarrow \mathbb{R}^3$ as our objects of interest. It is also possible to treat them as discrete approximations of a (Lipschitz) Gauss map $N : D \rightarrow S^2$ (resp. $C^{1,1}$ immersion $r : D \rightarrow \mathbb{R}^3$) as were considered in §3. With finitely many, isolated, branch points the passage to the continuous limit upon refinement of the quadmesh Q^ϵ follows from a straightforward application of standard arguments that are outlined in [17, §5.5]. As a “fully discrete” alternative we can also build approximations to the branched surface using hyperboloid surface patches since our quadmeshes are checkerboard colorable [51].

4.1. DDG on the Poincaré Disk. Thus far, we have constructed branched pseudospherical surfaces as A -nets, i.e mappings $r : Q^\epsilon \rightarrow \mathbb{R}^3$ from asymptotic coordinates into \mathbb{R}^3 . However, the primary object of interest in elasticity is the deformation $y : \Omega \rightarrow \mathbb{R}^3$, the mapping from the Lagrangian (material) domain Ω to the Eulerian (lab) frame \mathbb{R}^3 . To construct this mapping, we need also to compute the transformation $\zeta : Q^\epsilon \rightarrow \Omega$ that allows us to identify the material location corresponding to a point with given asymptotic coordinates. To this end, we start with a coordinatization of Ω .

Since our interest is in pseudospherical surfaces, we have $\Omega \subset \mathbb{H}^2$, and we can identify \mathbb{H}^2 with the Poincaré disk (\mathbb{D}, g) given by $\mathbb{D} = \{z \mid |z| < 1\}$, the unit disk, and $g = \frac{4dzd\bar{z}}{1 - |z|^2}$

[4]. We record a few standard facts about the Poincaré disk model for \mathbb{H}^2 :

(A) The distance between two points $z_1, z_2 \in \mathbb{D}$ is given by

$$d_{\mathbb{H}^2}(z_1, z_2) = \operatorname{arccosh} \left(1 + 2 \frac{|z_1 - z_2|^2}{(1 - |z_1|^2)(1 - |z_2|^2)} \right),$$

In particular, if one of the points is the origin, this expression reduces to

$$(4.8) \quad d_{\mathbb{H}^2}(0, z) = 2 \operatorname{arctanh}(|z|).$$

(B) The orientation preserving isometries of \mathbb{H}^2 are given by (a subgroup of) the Möbius transformations

$$(4.9) \quad f(z; z_0, \theta) = e^{i\theta} \frac{z + z_0}{1 + z\bar{z}_0}$$

where $|z_0| < 1, \theta \in [0, 2\pi)$. For our purposes, it suffices to take $\theta = 0$ and we shall henceforth drop this variable and use $f(z; z_0) = \frac{z+z_0}{1+z\bar{z}_0}$. It is straightforward to check that $f'(0; z_0) = 1 - |z_0|^2$ is real and positive, and $f^{-1}(w; z_0) = f(w; -z_0) = \frac{w-\bar{z}_0}{1-w\bar{z}_0}$.

(C) The discretized geodesics through $z = 0$ are given by $\gamma_\beta(n) = e^{i\beta} \tanh\left(\frac{n\Delta}{2}\right)$, where Δ is the separation between successive points on the geodesic. The geodesics through a point z_0 are given by composing with a Möbius transformation: $z_n = f(\gamma_\beta(n); z_0)$.

As we argued above, constructing the appropriate DDG for $K = -1$ surfaces is equivalent to constructing discrete Chebyshev nets, i.e rhombic quadrilaterals in the appropriate space. Constructing such rhombii on S^2 , as in (4.6), gives us DDG for the Gauss Normal map. As

we now show, the same idea also applies to the problem of finding the (discrete) mapping $\zeta : Q^\epsilon \rightarrow \Omega \subset \mathbb{H}^2$. Given ζ_0, ζ_1 and ζ_2 with $d_{\mathbb{H}^2}(\zeta_0, \zeta_1) = d_{\mathbb{H}^2}(\zeta_0, \zeta_2) = 2 \tanh\left(\frac{\Delta}{2}\right)$, we can apply the isometry $f(\cdot, -\zeta_0)$ to these points and obtain

$$w_j = f(\zeta_j, -\zeta_0), \quad w_0 = 0, \quad w_1 = \frac{\Delta}{2} e^{i\beta_1}, \quad w_2 = \frac{\Delta}{2} e^{i\beta_2}.$$

The fourth vertex w_{12} of the “normalized” rhombus diagonally across from the vertex w_0 at the origin, can be determine by a straightforward computation after setting $d_{\mathbb{H}^2}(w_{12}, w_1) = d_{\mathbb{H}^2}(w_{12}, w_2) = 2 \tanh\left(\frac{\Delta}{2}\right)$. ζ_{12} is then obtained by applying the inverse mapping $f(\cdot, \zeta_0)$. Putting everything together, we have

$$(4.10) \quad \begin{aligned} w_j &= f(\zeta_j, -\zeta_0) \quad i = 0, 1, 2 \\ w_{12} &= \frac{w_1 + w_2}{1 + |w_1 w_2|}, \\ \zeta_{12} &= f(w_{12}, \zeta_0) \end{aligned}$$

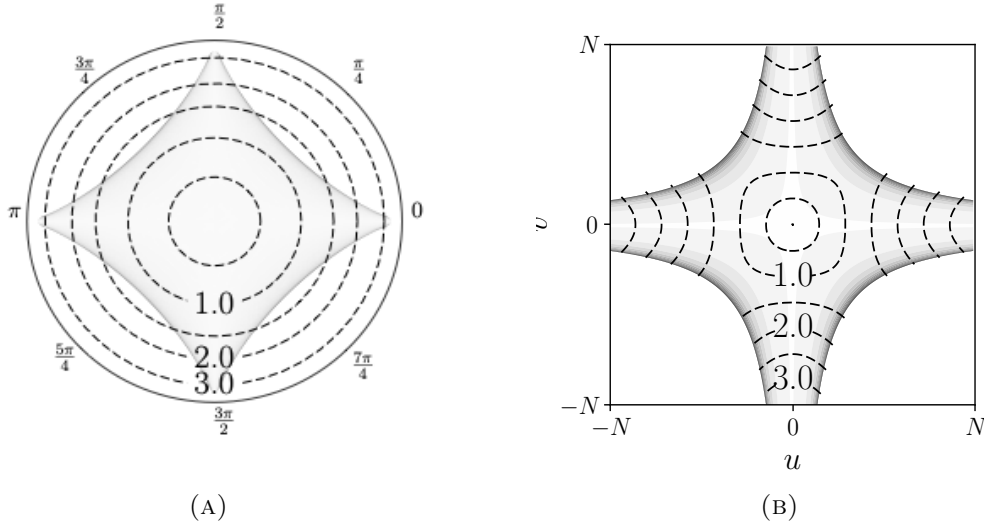


FIGURE 15. Examples of a piece of an Amsler surface represented in (a) asymptotic coordinates (u, v) and (b) in the Poincaré disk z , up to the singular edge, colored by the angle ϕ and contoured by geodesic radius with labels.

It is now straightforward to construct (branched) Chebyshev nets in \mathbb{H}^2 that inherit their topology from a given asymptotic skeleton. More formally, a discrete hyperbolic Chebyshev net is a quadgraph in \mathbb{H}^2 with an assignment of u and v labels to the edges such that each face (quad) has two u and two v edges which alternate, and satisfying (4.10) on each quad, where ζ_0 and ζ_{12} are one set of non-adjacent vertices, and ζ_1, ζ_2 are the vertices on the other diagonal. A branch point is any interior vertex with degree $2m \geq 6$. From the

Chebyshev net in \mathbb{H}^2 , we can immediately construct the corresponding A -net (discretized surface) in \mathbb{R}^3 by requiring that each star (the edges incident on a vertex $r_{j,k}$) be planar with lengths and angles given by the Chebyshev net at the vertex $\zeta_{j,k}$, i.e. the mapping between the Poincaré disk and \mathbb{R}^3 is a local isometry at each vertex. This mapping between the Poincaré disk and \mathbb{R}^3 is the desired Lagrangian to Eulerian map. Although the details, and the underlying equations are different, a related approach was used to investigate the wavy edges of leaves by mapping triangles in the Poincaré disk [75, 76].

As an illustration of our approach, we construct a discrete hyperbolic Chebyshev net corresponding to an Amsler surface with an angle $\varphi = \pi/2$ between the straight asymptotic lines where they intersect. Since these asymptotic lines are also geodesics in \mathbb{R}^3 , the same is true for the corresponding curves in the Poincaré disk. We pick the origin $z = 0$ to correspond to this point of intersection. If the rhombii have a side-length Δ it follows that the ‘Amsler-type’ boundary data on the Poincaré disk are given by $\zeta_{j,0} = \tanh\left(\frac{j\Delta}{2}\right)$, $\zeta_{0,k} = i \tanh\left(\frac{k\Delta}{2}\right)$. We then solve for $\zeta_{j,k}$ with $j \neq 0, k \neq 0$ using (4.10). The (discretized) angle between the asymptotic lines at node j, k is given by $\varphi_{j,k} = \arg(w_2 w_1^*)$ where the w_j are determined by (4.10) with $\zeta_0 = \zeta_{j,k}$, $\zeta_1 = \zeta_{(j+1),k}$, $\zeta_2 = \zeta_{j,(k+1)}$.

The results are displayed in Figure 15. Fig. 15a shows the hyperbolic Chebyshev net $\zeta_{j,k}$ where each node is colored by the angle $\varphi_{j,k}$ up to the contour $\varphi = \pi$ corresponding to the singular edge. The dashed curves are the boundaries of geodesic disks, labelled by radius. It is clear that the Amsler surface with angle $\pi/2$ allows us to smoothly embed hyperbolic disks of radius 1 into \mathbb{R}^3 but not a disk of radius 1.5 [38]. Fig. 15b displays the same information in terms of the discrete indices j, k which are proxies for the asymptotic coordinates u and v . Since the geodesic distance to the origin is easily computed in the Poincaré disk by (4.8), we have an efficient method to determine geodesic radii on pseudospherical surfaces without explicitly integrating the arclength [38] or solving an eikonal equation on the surface. Fig. 16 shows the corresponding A -net in \mathbb{R}^3 , a discretization of the Amsler surface with angle $\frac{\pi}{2}$ between the generators. Three separate singular edges are discernible.

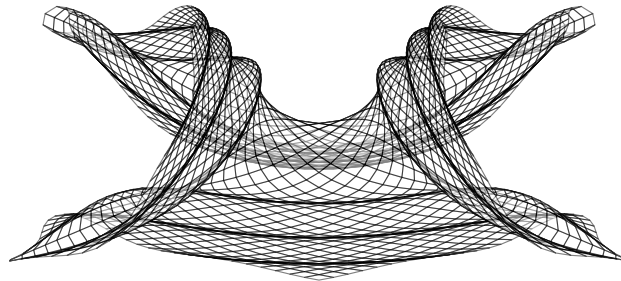


FIGURE 16. The Amsler surface with $\varphi_0 = \frac{\pi}{2}$.

The last notion we need to introduce is that of a *reversal*. We know that, in general, a pseudospherical parametrization $r(u, v)$ does not correspond to an immersed surface, and

the failure of (local) injectivity is associated with the locus where $\partial_u r \times \partial_v r = 0$. The notion of reversal captures this idea in a discrete setting. Let ω be an orientation on \mathbb{H}^2 . If $\zeta_{j,k}$ is a regular point, it is incident on 4 quads given by $\zeta_{j+p,k+q}$, where $p, q \in \{-1, 0, 1\}$. We say that there is a reversal at $\zeta_{j,k}$ if

$$(4.11) \quad \prod_{p \in \{-1,1\}, q \in \{-1,1\}} \omega(f(\zeta_{j+p,k}, -\zeta_{j,k}), f(\zeta_{j,k+q}, -\zeta_{j,k})) \leq 0.$$

This condition is invariant under Möbius transformations and also under reversal of the orientation $\omega \rightarrow -\omega$ being a product of 4 terms. The import of this condition is that, at a reversal one of the quads that is incident on $\zeta_{j,k}$ is flipped relative to the other three, so the Chebyshev net is folding over itself. The Amsler surface in Fig. 16 corresponds to three reversals of the associated hyperbolic Chebyshev net.

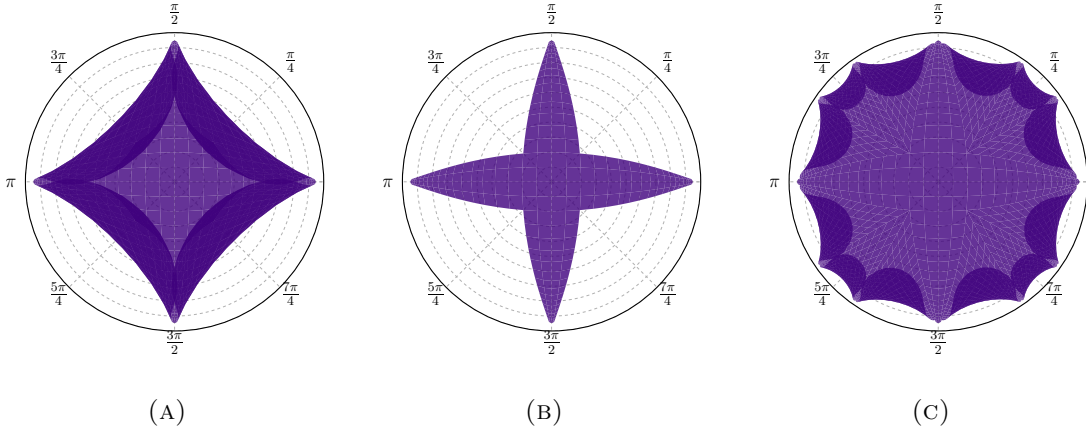
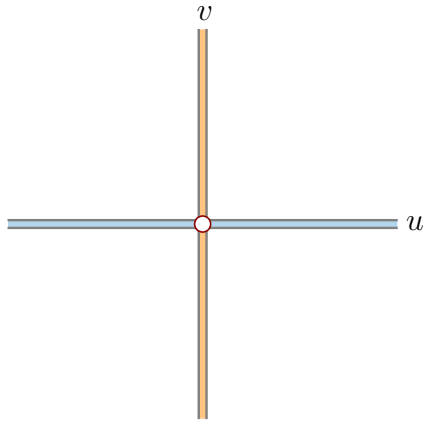
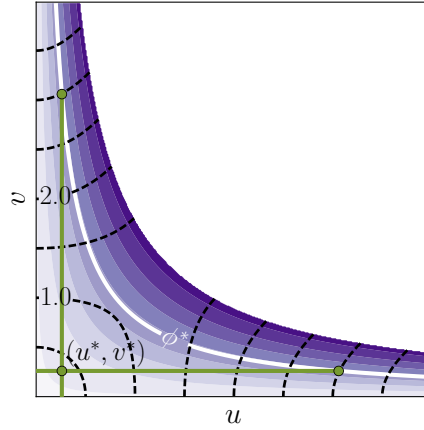


FIGURE 17. Introduction of branch points into the Poincaré disk via the surgical process. In (a) we see a smooth immersion, the singular edge inhibiting the ability to immerse a large portion of \mathbb{H}^2 ; (b) a cropped version and finally (c) the glued $C^{1,1}$ Poincaré disk. Overlapping “sheets” of the immersion appear significantly darker and provide a signature for the singular edge.

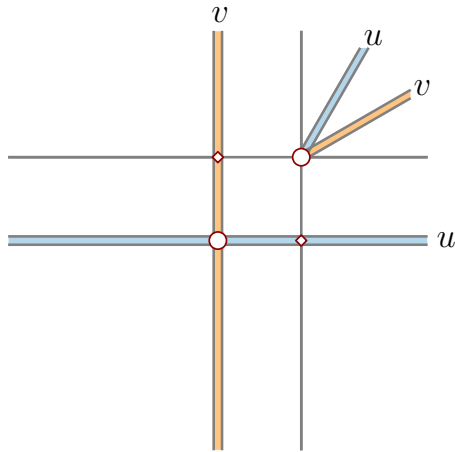
Fig. 17a shows the discrete hyperbolic Chebyshev net for the Amsler surface with angle $\pi/2$ ‘extended’ beyond the singular edge, where the Chebyshev net $\zeta_{j,k}$ appears to fold back upon itself, as expected. This is evident in Figure 17a. The rhombii in the Chebyshev net are colored with an opacity of eighty percent. As a result, overlapping “sheets” of the immersion appear significantly darker. Since our procedure gives a (discrete) isometry from the hyperbolic Chebyshev net to the corresponding A -net in \mathbb{R}^3 , a reversal in the hyperbolic Chebyshev net indicates that $\delta_u \zeta$ and $\delta_v \zeta$ have passed through collinearity. This corresponds to the angle φ between the asymptotic curves becoming 0 or π , indicating the occurrence of a singular edge.



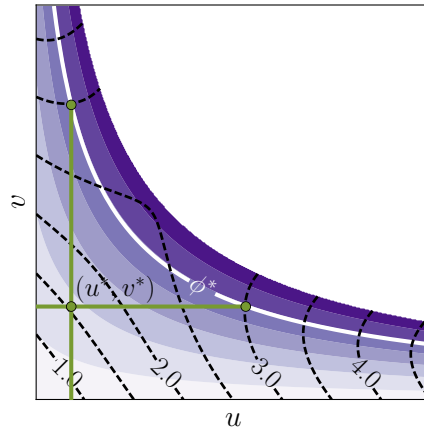
(A) Asymptotic skeleton at stage n



(B) Determining the cut location



(C) Asymptotic skeleton at stage $n + 1$



(D) Filling the cut and $n \rightarrow n + 1$.

FIGURE 18. Illustration of Algorithm 4.1. Desired $R = 3$. (a) The initial asymptotic curves on which we prescribe Amsler data (equally spaced points on geodesics) (b) Filling in the discrete hyperbolic Chebyshev net and identifying the first cut location (u^*, v^*) . (c) Introducing new asymptotic curves from the branch point on which we again prescribe Amsler data. (d) General sector having non-constant φ (non-Amsler data) along the v -axis. In (b),(d), the figures are colored by the value of φ with black-dashed contours representing geodesic radius, increments of 0.5. The solid green lines represent the edges of the L -cut, and their intersection the location of the branch point, (u^*, v^*) .

In Fig. 18 we show the steps for the particular example of starting with an Amsler surface with angle $\pi/2$ and building a (branched) immersion to $R = 3$, a radius beyond the initial singular edge. To stave off the singular edge we first pick a threshold angle $\phi^* < \pi$. For the illustration in Fig. 18 we take $\phi^* = 3\pi/4$. We then excise the region $u \geq u^*, v \geq v^*$, where u^*, v^* are determined by the intersection of the geodesic circle with radius $R = 3$ with the contour $\varphi(u, v) = \phi^*$. Note that, at this point $\varphi(u^*, v^*) \equiv \varphi^* < \phi^* < \pi$ and $R < 0.5$, so the cut is *significantly inside* the singular edge of the initial Amsler surface.

We now perform *surgery* to replace the removed sector by 3 new sectors. This needs the introduction of two more asymptotic curves, indicated in Fig. 18c, along which we are free to prescribe data. We prescribe this data in the Poincaré disk by picking equally spaced point on the two geodesics through the point $\zeta_0 = \zeta(u^*, v^*)$ obtained by trisecting the angle left behind by the sector that is removed. In more detail, if w_1 and w_2 are the “edges” of the excised sector, moved to the origin by a Möbius transformation (See (4.10)), we define $\varphi_1 = \arg(w_2 w_1^2)/3, \varphi_2 = \arg(w_2^2 w_1)/3$. Then, the appropriate geodesics are given by undoing the Möbius transformation,

$$(4.12) \quad \zeta_{0,k} = f \left(e^{i\varphi_1} \tanh \left(\frac{k\Delta}{2} \right), \zeta_0 \right), \quad \zeta_{j,0} = f \left(e^{i\varphi_2} \tanh \left(\frac{j\Delta}{2} \right), \zeta_0 \right),$$

where Δ is the side-length of the rhombii in the Chebyshev net. The three new sectors in Chebyshev net can then be “filled in”, i.e. we can determine $\zeta_{j,k}$ in their interiors, using (4.10). We can do this in each of the 4 sectors (quadrants) that constitute the initial Amsler surface and the resulting Chebyshev net in the Poincaré disk is illustrated in Fig. 17c. The result is a discrete Chebyshev net with 4 vertices of degree 6, one in each quadrant, corresponding to the branch points. We thus have implemented surgery, as introduced in §3.3, directly in the Poincaré disk.

Fig. 18d shows one of the resulting sectors in the 2nd generation, i.e. the asymptotic curves defining the boundaries of the sector are incident on the branch point (u^*, v^*) from the first cut. Note that the singular edge again intersects the geodesic circle $R = 3$ so we have to repeat the entire procedure to obtain the 2nd generation branch points and 3rd generation sectors. Note also that the new branch point is at $R \approx 1.5$ and thus the first and second generations sectors, taken together, are closer to covering the desired domain $R \leq 3$, and do so while maintaining $\varphi \leq \phi^*$ everywhere.

This *surgery* procedure can be repeated recursively to construct branched isometric immersions of arbitrarily large hyperbolic disks. We list the steps involved in Algorithm 4.1. This is a ‘greedy’ algorithm for constructing branched immersions since it is based on picking the cut locations using information local to a particular sector, and attempts to maximize the size of the sector in the current generation, rather than pick the cut location in a more globally optimal fashion (See §5.3). By construction, the algorithm generates distributed branch points in a recursive and self-similar manner, We discuss this further in §5.1, where we estimate the number of recursion steps needed before the algorithm terminates when applied to a hyperbolic disk with (geodesic) radius R . Fig. 19 illustrates the final step in Algorithm 4.1, showing discrete surfaces constructed from mapping the rhombii in hyperbolic Chebyshev nets to skew rhombii in \mathbb{R}^3 .

Algorithm 4.1 A greedy algorithm for building large branched surfaces recursively.

- 1: **Parameters:** Radius R of disk to be embedded, cutoff angle $\pi/2 < \phi^* < \pi$.
 - 2: **Initialize:** $\zeta_{j,k}^0 \leftarrow$ hyperbolic Chebyshev net for Amsler surface, $\varphi_0 = \frac{\pi}{2}$.
 - 3: Discard points in $\zeta_{j,k}$ outside the geodesic disk or radius R .
 - 4: sectors = $\{\Omega_1, \Omega_2, \Omega_3, \Omega_4\}$ given by the 4 quadrants.
 - 5: **repeat**
 - 6: Identify a sector Ω_i containing points with $\varphi_{j,k} > \phi^*$.
 - 7: $j^* \leftarrow \max\{j \mid \varphi_{n,k} \leq \phi^* \forall \zeta_{n,k} \in \Omega_i, n \leq j\}$.
 - 8: $k^* \leftarrow \max\{k \mid \varphi_{j,n} \leq \phi^* \forall \zeta_{j,n} \in \Omega_i, n \leq k\}$.
 - 9: Remove the points $\zeta_{j,k}, j > j^*, k > k^*$ from Ω_i .
 - 10: Add new asymptotic curves using geodesics using (4.12) to out beyond radius R .
 - 11: Add three new sectors using (4.10).
 - 12: Discard points in $\zeta_{j,k}$ outside the geodesic disk of radius R .
 - 13: **until** no sector contains points with $\varphi_{j,k} > \phi^*$.
 - 14: $Q =$ quadgraph given by the hyperbolic Chebyshev net $\zeta_{j,k}$.
 - 15: Construct an A -net $r : Q \rightarrow \mathbb{R}^3$ using the side-lengths and angles determined from $\zeta_{j,k}$.
-

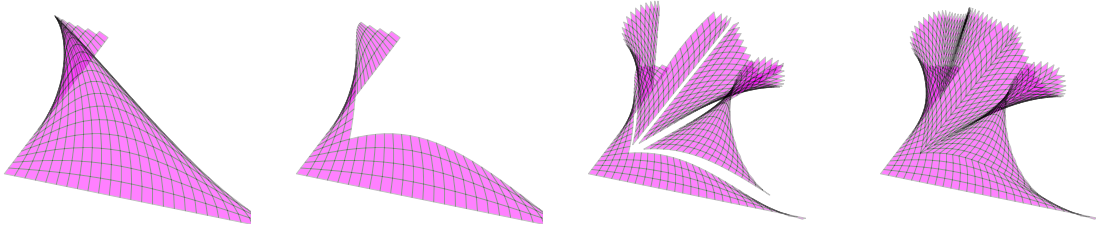


FIGURE 19. The process of constructing a discrete isometric immersion recursively by surgery. These figures illustrate the generation an A -net in \mathbb{R}^3 from a discrete Chebyshev net in the Poincaré disk.

There is an alternative, “non-recursive”, construction for isometric immersions of hyperbolic disks into \mathbb{R}^3 , that is achieved through sufficiently narrow Amsler sectors, whose singular edges are further away from the origin than the radius R , meet a single branch point of sufficiently high index at the origin [38, 40]. The comparison between the two methods is shown in Fig. 20. The figures show the discrete Chebyshev net in \mathbb{H}^2 corresponding to the recursive and single branch point isometries of hyperbolic disks of radii 2, 3 and 4 respectively. The quads in the Chebyshev nets are colored by the κ_{\max} , the larger principal curvature. It is clear that the energies of both types of embeddings grow with R , the radius of the hyperbolic disk, but the energy of recursive embeddings grows slowly compared to the energy of single branch point ‘periodic-Amsler’ embeddings.

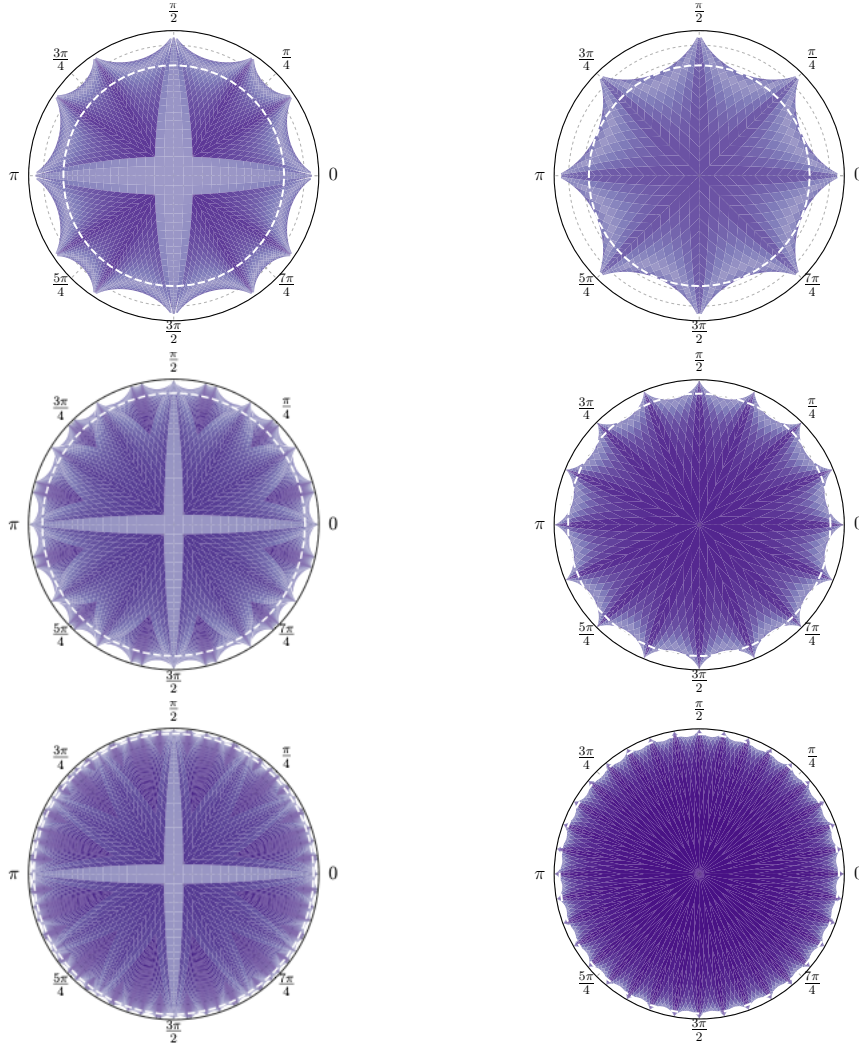


FIGURE 20. A comparison of isometric immersions of \mathbb{H}^2 via recursively constructed branched surfaces (left) and by a single branch point at the origin with a large index (right) as represented in the Poincaré disk. The figures show immersions with geodesic radii $R = 2, 3$ and 4 represented by the dashed line. The surfaces are colored by the max of the absolute principal curvatures: darker representing higher energy.

5. DISTRIBUTED BRANCH POINTS IN APPLICATIONS

We now investigate the energies of the various classes of pseudospherical immersions. The principal curvatures are determined by the angle $\varphi(u, v)$ between the asymptotic directions as $\kappa_1 = \pm \tan \frac{\varphi}{2}, \kappa_2 = \mp \cot \frac{\varphi}{2}$. Consequently, the bending energy (both $W^{2,\infty}$ and $W^{2,2}$)

diverge if the singular edge $\varphi = 0$ or $\varphi = \pi$ encroaches the domain $\Omega \subset \mathbb{H}^2$. Our goal therefore is to construct immersions of Ω such that the angle φ between the asymptotic lines satisfies $0 < \delta \leq \varphi \leq \pi - \delta < \pi$, where $\delta = \delta(\Omega) > 0$, and gives a quantitative measure of how “non-singular” we can make an isometric immersion $\Omega \subset \mathbb{H}^2 \rightarrow \mathbb{R}^3$.

For C^2 pseudospherical surfaces, earlier analysis suggests that the optimal shapes (immersions) that maximize δ are given by Minding’s bobbin [38]. Minding’s bobbin is a surface of revolution given in cylindrical polar coordinates (ρ, θ, z) by $\rho(s) = \rho_0 \cosh(s)$, $z(0) = 0$, $z'(s)^2 + \rho'(s)^2 = 1$, where s is the arclength along a meridian from the equator and ρ_0 is a constant, that is related to δ , the quantitative measure of smoothness [38] of the immersion. The maximal extension of Minding’s bobbin has a singular edge at a finite distance from the equator, since it cannot be extended beyond the finite value(s) of s where $\rho'(s) = \pm 1$.

Explicitly computing the associated $W^{2,\infty}$ energy as a function of desired geodesic radius R (arclength from the equator) of the surface [38] we obtain: $\mathcal{E}_{MB} = C_1 e^{C_2 R} + O(1)$. Moreover, numerical evidence in [38] suggests this scaling holds for all C^2 isometric immersions of hyperbolic domains that contain a disk of radius R . Recalling our definitions of the optimal energies for various classes of isometries,

$$\begin{aligned} \mathcal{E}_R^2 &= \inf \{ \mathcal{E}(r) : r : B_R \rightarrow \mathbb{R}^3 \text{ is a } C^2 \text{ isometry} \}, \\ \mathcal{E}_R^{\text{bs}} &= \inf \{ \mathcal{E}(r) : r : B_R \rightarrow \mathbb{R}^3 \text{ is a piecewise } C^2 \text{ isometry with isolated branch points} \}, \\ \mathcal{E}_R^{1,1} &= \inf \{ \mathcal{E}(r) : r : B_R \rightarrow \mathbb{R}^3 \text{ is a } C^{1,1} \text{ isometry} \}. \end{aligned}$$

we have

$$(5.1) \quad \log \mathcal{E}_R^2 \sim R$$

Alternative low energy immersions of hyperbolic disks are in the form of $C^{1,1}$ periodic Amsler surfaces [38, 40] which introduce a single branch point at the origin. Even with the introduction of this branch point, there are still “large” sets, in particular, disks with radius $R/2$ which are free of branch points and where the immersion is smooth (or can be approximated by smooth isometries as discussed in Remark 3.9), so Eq. 5.1 implies that, even for these periodic Amsler surfaces, $\log \mathcal{E} \sim R$.

Our construction (Algorithm 4.1) introduces distributed branch points, which appear “as needed”. In this case, as we argue below, we stave off the singular edge and obtain an energy scaling

$$(5.2) \quad \log \mathcal{E}_R^{\text{bs}} \sim \sqrt{R},$$

achieving an improvement in the scaling of the *logarithm of elastic (bending) energy*. The difference between the energy scales of the smooth and branched isometries is enormous – For any $\epsilon > 0$, $\mathcal{E}_R^{\text{bs}} \ll (\mathcal{E}_R^2)^\epsilon$ for all sufficiently large R . The number of generations of branch points, which we call the *cut depth*, grows linearly with the radius R of the disk.

While we do not have rigorous proofs for these claims yet, we give arguments that illustrate the intuition behind these relations in §5.1. We also have numerical evidence for the energy and cut depth scaling obtained from Algorithm 4.1 applied to hyperbolic disks of radius up to 10. Figure 21a shows the analytically derived energy scaling for Minding’s

bobbin, conjectured as the minimizer of the elastic energy over the class of all C^2 isometric immersions, as in (5.1). Periodic-Amsler surfaces exhibit a similar $\exp(R)$ scaling, though with an improved constant [38]. The energetic benefits of introducing distributed branch points is clear, with an apparent energy scaling $\exp(c\sqrt{R})$. The cut depth scales linearly with R as shown in Figure 21b. Fig. 21c shows an immersed pseudospherical surfaces with distributed branch points, a mathematical ‘hyperbolic crochet’ with $R = 3$.

5.1. Recursion on Amsler type surfaces. Amsler surfaces play a fundamental role in our construction, and in particular *Amsler sectors*: the (partial) pseudospherical immersions associated with a single quadrant in the uv -plane and data $\varphi(u, 0) = \varphi(0, v) = \phi_0$. Amsler surfaces are constructed from self-similar solutions of sine-Gordon of the form $\varphi(u, v) = \varphi(z)$, with $z = 2\sqrt{uv}$. Substitution immediately gives $\partial_{uv} = \frac{1}{z}\partial_z + \frac{\partial^2}{\partial z^2}$ and the sine-Gordon equation transforms into

$$(5.3) \quad \varphi''(z) + \frac{\varphi'(z)}{z} - \sin \varphi(z) = 0,$$

known as Painlevé III in trigonometric form [13]. The preimage of $z = 0$ is the set $\{(u, v) : u = 0 \text{ or } v = 0\}$, and hence we see immediately that $\varphi(u, v)$ is a constant along the axes.

The large z asymptotics for solutions of the Painlevé III ((A.5) in Appendix A) yields:

$$(5.4) \quad \varphi(z) \approx \varphi_0 \frac{e^z}{\sqrt{2\pi z}} \quad \text{for } 1 \ll z \lesssim -\log(\varphi_0),$$

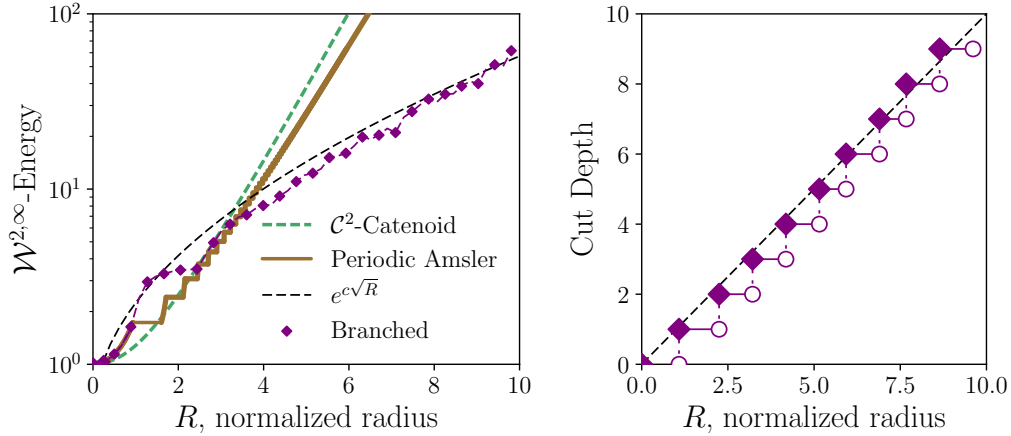
where φ_0 is the angle between the intersecting straight asymptotic lines that determine the Amsler sector. This expression is valid for $z \lesssim z^* \simeq -\log(\varphi_0)$.

Algorithm 4.1 is a recursive process that requires us to make cuts along asymptotic curves to excise all regions within the domain where the angle between the asymptotic directions is larger than a threshold ϕ^* . We will use ϕ_n to denote the initial angle for an n^{th} generation branch point, and let s_n denote the distance to the boundary, i.e the distance left to cover at the n^{th} step of the iteration.

Since we start with an Amsler surface with angle $\frac{\pi}{2}$, we have $\phi_0 = \frac{\pi}{2}$, $s_0 = R$ at the start of the recursion. To avoid the singular edge, we pick a threshold angle $\phi^* \leq \pi - \delta$. The critical curve is given by the contour $\varphi^{-1}(\phi^*)$. For Amsler sectors, $\varphi = \varphi(z)$ and Eq. (5.4) gives the asymptotic expansion for $2\sqrt{uv} = z^* = \varphi^{-1}(\phi^*)$ as

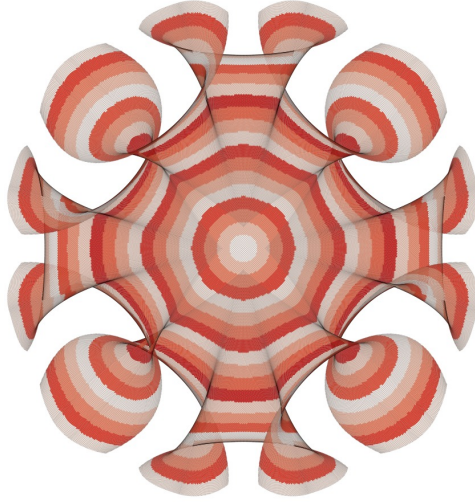
$$(5.5) \quad z^* \approx \log \frac{\phi^*}{\phi_n} + \frac{1}{2} \log(2\pi) + \frac{1}{2} \log \left(\log \left(\frac{\phi^*}{\phi_n} \right) + C \right) \dots$$

The recursion process analyzed below involves selecting a branch point (u_n^*, v_n^*) and a cutoff angle, ϕ^* . For specificity one may take $\phi^* = \frac{3\pi}{4}$. Consider an Amsler surface with angle $\phi_n = \varphi(0, 0)$ at the origin which we hope to use to construct an immersion of geodesic radius s_n . Once a branch point is selected, we trisect the angle $\varphi(u^*, v^*)$ to get the angle $\phi_{n+1} = \frac{\varphi(u^*, v^*)}{3}$ which will be used for the $(n+1)^{\text{th}}$ generation. We thus have a recursive dynamical system for two quantities: the angle ϕ_n at the origin of the n^{th} generation and the distance to the boundary s_n , that is yet to be covered. A schematic of the procedure is illustrated in Figure 22a.



(A)

(B)



(c)

FIGURE 21. (a) The $W^{2,\infty}$ elastic energy for immersions of three types: Minding's bobbins (C^2 -catenoid, thick-dashed), $C^{1,1}$ periodic-Amsler surfaces (solid) and $C^{1,1}$ branched surfaces (dashed-diamond), as well as the reference $e^{\frac{3}{2}\sqrt{R}}$ on a logarithmic scale. (b) The maximum recursion depth n as a function of the geodesic radius R . (c) A numerically generated 'hyperbolic crochet'. The immersion is obtained using Alg. 4.1 on a disk of radius $R = 3$. The stripes indicate the geodesic distance to the center.

For Amsler surfaces the u -axis is a geodesic, and assuming that the cut node is near to the origin, we set $\tilde{u} \approx s_n$ and $z^* = 2\sqrt{u_n^* s_n}$. It immediately follows from (5.5) that

$$(5.6) \quad u_n^* = v_n^* = \left(\frac{\log(\phi^*/\phi_n)}{2\sqrt{s_n}} \right)^2.$$

This estimate is rigorous for Amsler sectors, i.e. sectors with both boundaries are given by geodesics. In our recursion, we also get sectors where only one boundary is a geodesic, and the other is a curve with nonzero geodesic curvature that is prescribed by the need to patch on to a neighboring sector. In this case, we expect that $u_n^* \neq v_n^*$, as in Fig. 18d, but (5.6) is nonetheless approximately true.

For the relevant values of z : $z^* \gg 1$ and $\sqrt{u_n^* v_n^*} \ll 1$, the metric along $u = v$ allow us to write an expression for the dynamics of s_n

$$ds^2 = (2 + 2 \cos \varphi) du^2 = 4 \cos^2 \frac{\varphi}{2} du^2,$$

leading to the inequality

$$(5.7) \quad s_n - 2\alpha^2 \cos \frac{\phi_n}{2} \leq s_{n+1} \leq s_n - \int_0^{u_{n+1}} ds.$$

Substituting u_n^* and v_n^* into the asymptotic expression for φ for small z (see Eq. (A.5)), we obtain the recursion relations:

$$(5.8) \quad \alpha = \frac{1}{\sqrt{s_n}} \log \left(\frac{\phi_n^*}{\phi_n} \right), \quad \phi_{n+1} \simeq \frac{\phi_n}{3} \left(1 + \frac{\alpha^4}{4} \right), \quad s_{n+1} \simeq s_n - 2\alpha^2 \cos \frac{\phi_n}{2}.$$

We have implemented Algorithm 4.1 on geodesic disks of radii $1, 2, \dots, 10$. At every cut (u^*, v^*) we record the ratio $\frac{\phi_{n+1}}{\phi_n}$ relating the opening angles of the daughter sectors to the angle of the parent sector. We also record and the quantity α defined in (5.8). This data is displayed as ellipses with twenty percent opacity in Fig. 22b. We have also plotted the curve given by the function $\left(1 + \frac{\alpha^4}{4}\right)$. This curve is indeed a “frontier” in that all the numerical data for $\frac{\phi_{n+1}}{\phi_n}$ lie on or above this curve. This validates the recursion relations (5.8), which we motivated by considering Amsler sectors, as inequalities applicable to more general sectors (where not both edges are geodesics).

The crude bound $s_n \leq R$ gives

$$s_n \leq R, \quad \alpha \geq \frac{1}{2\sqrt{R}} \log \left(\frac{\phi_n^*}{\phi_n} \right), \quad \phi_{n+1} \geq \frac{\phi_n}{3} \left(1 + \frac{\alpha^4}{4} \right),$$

If $\frac{1}{2\sqrt{R}} \log \frac{\phi_n^*}{\phi_{\min}} \equiv \alpha^* \geq 2$, it follows that $\phi_{n+1} \gtrsim \min(\phi_n, \phi_{\min})$. It therefore suffices to pick

$$(5.9) \quad \phi_{\min} \approx \exp(-C_2 \sqrt{R}).$$

This condition guarantees that $\alpha \geq \alpha^*$ is large enough so that $\frac{\phi_{n+1}}{\phi_n} \geq \frac{1}{3} \left(1 + \frac{(\alpha^*)^4}{4} \right) > 1$ if $\phi_n \simeq \phi_{\min}$. Consequently, the recursion cannot drive ϕ_n below ϕ_{\min} if we start with $\phi_0 > \phi_{\min}$. Numerically, we find that $C_2 \approx \frac{3}{2}$.

For our recursively generated surfaces, we start with an initial “symmetric” Amsler surface that has $\phi_0 = \frac{\pi}{2}$ which is greater than ϕ_{\min} in (5.9) for all $R \geq 0$. ϕ_{\min} directly gives an upper bound for the $W^{2,\infty}$ -norm of the surface – $\phi_{\min} \leq \phi \leq \phi^*$ is bounded strictly

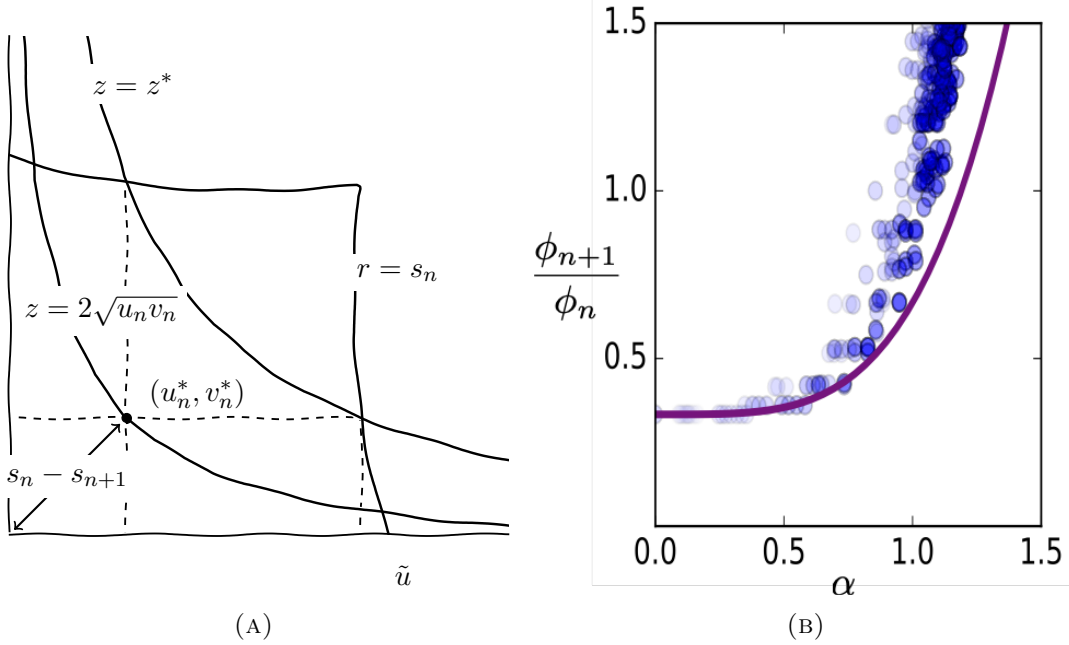


FIGURE 22. (a) Annotated illustration of an L-shaped cut in going from the n^{th} to the $n + 1^{\text{th}}$ generation. (b) A scatter plot of $\frac{\phi_{n+1}}{\phi_n}$ vs. α for immersions, of multiple radii, generated by Alg. 4.1

away from π means we can estimate the energy as no greater than:

$$(5.10) \quad \mathcal{E} = \sup_{x \in B_R} \max(|\kappa_1(x)|, |\kappa_2(x)|) \lesssim \max\left(\cot \frac{\phi_{\min}}{2}, \tan \frac{\phi^*}{2}\right) \approx C_1 \exp\left(C_2 \sqrt{R}\right),$$

for sufficiently large R , which is our claimed energy bound, Eq. (5.2), for isometries with branch points.

From the bound (5.10) on \mathcal{E} and the estimate in (5.1) for C^2 patches devoid of branch points, it follows that we cannot have a region of size about \sqrt{R} that is free of branch points. The area of a hyperbolic disk with radius R scales like $\exp(R)$ while the “largest” size of regions free of branch points can only be $\exp(\sqrt{R})$. Consequently, we get that the number of branch points scales like $\exp(R - \sqrt{R})$. Since each parent has 3 daughter branch points in Algorithm 4.1, the number of branch points grows exponentially with the number of generations, and it follows that the cut depth scales like

$$n \sim \max(R - \sqrt{R}, 0),$$

corresponding to a function “nearly” linear function whose slope increases slowly, precisely as we observe in Fig. 21b.

5.2. Growing leaves and distributed branch points. Thus far we have considered the “static” problem described in (3.1), i.e. there are no dynamics and the system is time independent. A natural extension of our discussion thus far is to consider problems where the geometry and/or the domain is changing with time, a process we will call *growth*. A particular case, which is relevant to the growth of leaves, is to the problem of low energy immersions of a “time-dependent” domain $\Omega(t) \subseteq \mathbb{H}^2$.

A growing thin sheet would like to maintain isometry at all times. As the sheet grows to be sufficiently large, it will become energetically favorable for the sheet to introduce branch points and refine its buckling pattern. Finally, the sheet would like to do this only with local/continuous changes to geometry, rather than global shape transitions.

An idealized example of a growing sheet is a “circular leaf” given by $\Omega(t) = \{z \mid |z| \leq \frac{1}{2} \tanh(t)\} \subseteq \mathbb{H}^2$, i.e. a hyperbolic disk with radius $R(t) = t$. As we saw above, one possibility is to have a single branch point at the origin with an index (order of saddleness) $m(t)$ that is increasing in time. Since $m(t)$ is discrete, it will be necessarily discontinuous in time if we seek to maintain sectors of equal angular widths for all time. Also, the geometry changes globally and discontinuously at the transition $m \rightarrow m + 1$.

On the other hand, for the recursive branch point construction, Alg. 4.1, branch points enter the domain through the boundary as needed, and they move towards the origin continuously in time. This effect is evident from Fig. 20 where we can see the location of the first cut, i.e the branch points $\zeta(u^*, v^*)$ closest to the origin, move inwards as the radius of the disk is increased. This effect is highlighted in Fig. 23, where points on the surface are colored by depth, i.e. the number of cuts/branch points that are antecedent to the asymptotic sector that contains the point.

Branch points entering through the boundary represents local shape deformations with changes in the asymptotic skeleton S . With a fixed S , changing the the embedding $S \rightarrow \Omega \subset \mathbb{H}^2$ moves the branch points within the material, and changes the (Eulerian) morphology of the sheet. Branch points are not material (Lagrangian) entities, and hyperbolic surfaces have a considerable amount of freedom. There are a large number of “floppy” bending modes from varying the embedding $S \rightarrow \Omega$. These two mechanisms, namely branch points entering through the boundary and moving relative to the material, are illustrated in Fig. 23, that show 2 generations of branch points entering through the boundary and migrating towards the center as the sheet grows.

5.3. Shape control through distributed branch points. The technological applications of thin elastic sheets is growing more rapidly than ever with the advent of elastomeric/hydrogel thin-films [55], flexible electronics [97] and soft robotics [57]. To utilize these new technologies, understanding how one may control the shape of these structures becomes imperative, and hyperbolic geometries represent a significant challenge because they are intrinsically very floppy.

We propose a novel idea in this context - *branch point engineering*, which we illustrate by means of an example. Consider a hyperbolic disk $B = B_1$ of radius $R = 1$ and intrinsic curvature $K = -1$. This disk can be isometrically embedded in \mathbb{R}^3 as a subset of the Amsler surface with $\phi_0 = \frac{\pi}{2}$. Imagine that we can engineer a branch point at a desired location

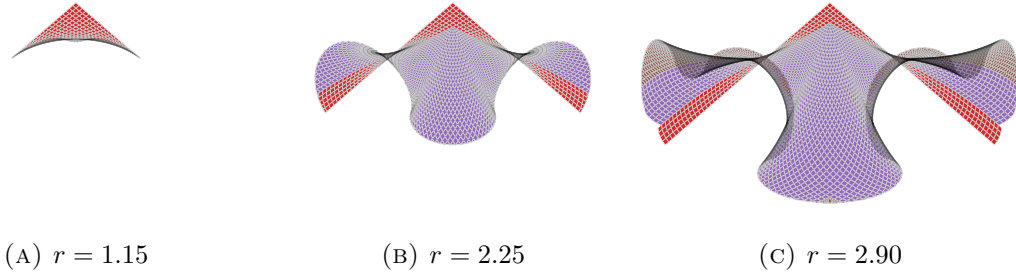


FIGURE 23. Frames from a growing surface showing the process by which branch points enter from the boundary in a continuous way. The surfaces are colored by cut depth.

along the diagonal (u^*, u^*) where the pre-existing angle $\varphi(u^*, u^*)$ is trisected among the daughter sectors. Since the original surface has 4 sectors, this will correspond to introducing 4 symmetrically placed branch points. This process is illuminated using Figure 24.

We have one control parameter, the geodesic radius $r^* = r(u^*, v^*)$ at the location of the branch point. For the resulting surface the total variation in the vertical coordinate, $\Delta z = z_{\max} - z_{\min}$ is a proxy for “shape.” Corresponding to each $r^* \in [0, 1]$ we also compute the bending ($W^{2,\infty}$) energy \mathcal{E} of the surface. The dependence of Δz and $\mathcal{E} \equiv \mathcal{E}_\infty$ on r^* are shown in Figure 25.

The $W^{2,2}$ energy $\mathcal{E}_2 = \int_B (\kappa_1^2 + \kappa_2^2)$ is bounded in terms of the $W^{2,\infty}$ energy $\mathcal{E}_\infty = \sup_B \max(|\kappa_1|, |\kappa_2|)$ by $\mathcal{E}_2 \lesssim 2A(B)\mathcal{E}_\infty^2$ where $A(B)$, the area of the unit disk, is $O(1)$. We can estimate the (physical) force resisting vertical compression by

$$(5.11) \quad F \approx -\frac{YR^2}{24} \left(\frac{h}{R}\right)^3 \frac{1}{R^{-1}} \frac{d\mathcal{E}_2}{d(\Delta z)} \simeq -\frac{YA(B)h^3\mathcal{E}}{6} \left(\frac{d(\Delta z)}{dr^*}\right)^{-1} \left(\frac{d\mathcal{E}}{dr^*}\right),$$

where Y is the elastic modulus of the material and h is the thickness of the sheet. The expression follows from recognizing that YR^2 is a force scale, \mathcal{E}_2 and $R^{-1}\Delta z$ are both dimensionless, and the physical elastic energy scales as h^3 with the thickness of the sheet.

Of course, the right hand side of (5.11) is only an estimate of the true force. Nonetheless, it is a useful expression for describing qualitative behavior. There is a wide plateau, between $r^* = 0$ and $r^* \approx 0.75$ where the energy changes very little despite an almost 7 fold change in Δz . The force in this regime resists compression but it is small, implying that the surface is very floppy. Between about $r^* = 0.75$ and $r^* = 0.9$ the force no longer resists compression, so the sheet is mechanically unstable and can act as a switch spontaneously generating forces on the scale Yh^3/R . Finally there is an outer region $r^* \gtrsim 0.9$ where the sheet acts as a “stiffer” spring in comparison to the regime $r^* \lesssim 0.75$. Also, the branch points couple differently with the vertical compression – for $r^* \lesssim 0.75$ vertical compression pushes the branch points inwards, while for $r^* > 0.9$ it pushes them outwards.

These are just a few examples of the nontrivial mechanical properties of hyperbolic sheets. This “extreme mechanics” can be exploited by controlling branch points, which,

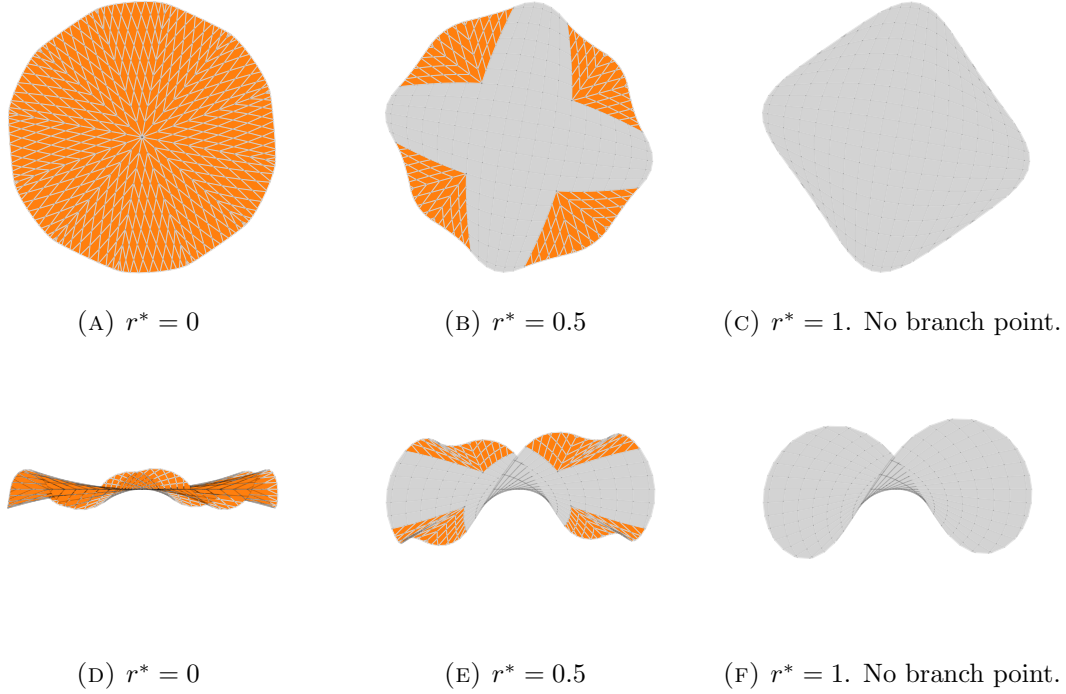


FIGURE 24. A sequence of $R = 1$ hyperbolic surfaces with varying locations for the cut location, in fractional radius, along the diagonal. The upper images (a-c) show the surfaces from above. The colored regions are the 2nd generation sectors. The lower images (d-f) are the inside view. The physical scales, in particular the vertical scales are the same for all the illustrations.

as we discussed above, are not tied to material points and can thus move “easily”. As we will discuss elsewhere these nonlinear mechanical properties are indeed exploited by a variety of biological systems. These mechanical properties can therefore confer evolutionary advantages to living organisms and thus contribute to the observed ubiquity of hyperbolic forms in nature [95].

As a final point of consideration, the discussion in this section is based on a hyperelastic model for the elastic sheet, *e.g.* Eq. (2.4), so that no energy is dissipated in moving a branch point through the material. More realistic models for moving branch points can be derived, in a thermodynamically consistent manner, using the continuum mechanical framework introduced in [2]. This makes connections with continuum mechanical descriptions of dissipation/plasticity that relate these phenomena to the motion of defects [90]. In particular, the theoretical ideas and numerical methods from [5] are potentially adaptable to our problem for a proper formulation and efficient computation of moving branch points with realistic dissipation mechanisms.

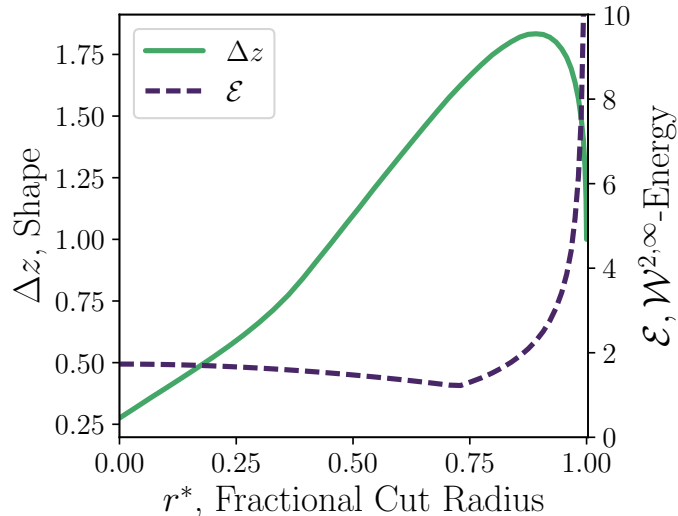


FIGURE 25. Total height, Δz as a function of fractional branch point location, $r^* = \frac{r(u^*, u^*)}{r_{\max}}$ (solid) and the corresponding elastic energy (dashed)

6. DISCUSSION

In this work we have outlined a theory for distributed branch points and their role in the geometry and mechanics of thin hyperbolic objects. Branch points are novel topological defects in $C^{1,1}$ hyperbolic surfaces, that confer a great deal of flexibility for the extrinsic geometry of the surface, i.e. allow significant shape changes, while preserving the intrinsic geometry, i.e. they do not concentrate stretching energy. They are unique in this aspect, since most other defects in condensed matter systems do concentrate energy.

In our view, these are some of the key results from this work –

- (1) We define a topological index for branch points and prove that it is “robust” (Theorem 3.8). Further, this index is necessarily zero for smooth hyperbolic surfaces, so it is an “obstruction” for numerical methods that rely on approximation by twice differentiable surfaces. Such methods will not, in general, adequately capture important aspects of the geometry/mechanics of thin hyperbolic sheets with branch points.
- (2) In §3.4, we connect the nontrivial topology induced by branch points to Thurston’s theory of measured foliations [91], specifically to *pairs of transverse measured foliations*. This naturally leads to the notion of an *asymptotic skeleton*. The asymptotic skeleton of a surface is a quadgraph, encoding an adjacency relation for branch points, that characterizes the topology of the corresponding Gauss normal map.

- (3) We prove a generalization of the sine-Gordon equation for surfaces with branch points in Theorem 3.13. As a consequence, we show that optimizing the bending energy among isometric immersions of hyperbolic surfaces naturally leads to distributed branch points (see Remark 3.14).
- (4) In §4.1 we develop a discrete differential geometric (DDG) theory for the basic object of interest in elasticity, the deformation map from the Lagrangian to the Eulerian frame. This DDG *does encode* the asymptotic skeleton and the topology of branch points *exactly*. Numerical methods based on this approach are guaranteed to converge to the right solution in the larger class of hyperbolic surfaces with branch points, rather than only for twice differentiable surfaces.
- (5) We formulate an algorithm, Alg. 4.1, to generate arbitrarily large hyperbolic surfaces with distributed branch points and (relatively) slower growth in the maximum curvature with the size of the domain, than for C^2 immersions.
- (6) We demonstrate an energy gap between branched and smooth pseudospherical surfaces. Our analysis also reveals a recursive/self-similar, fractal-like pattern in the distribution of branch points. This answers our motivating question – *Why do systems, with completely different physics, some directed by complex evolutionary processes and others generated by simple mathematical rules end up with similar fractal-like buckling patterns?*
- (7) Branch points are not material entities. For the hyperelastic models considered in this paper, they can move in the material with zero energy cost. We investigate the implications of this feature for growth (in §5.2) and novel mechanical properties (in §5.3) in hyperbolic sheets.

We now expand on item 6, which is the central motivating question for this work. Bounded subsets of smooth hyperbolic manifolds can always be embedded smoothly in \mathbb{R}^3 . Consequently, the candidate morphologies of hyperbolic sheets in the vanishing thickness limit are isometric immersions. There is no stretching energy, so the competition is between the two components of the principal curvature [36]. This is in contrast to other multi-scale phenomena in thin sheets [73] which are manifestly driven by a competition between stretching and bending energies [12, 67, 20, 92, 10, 77] or more generally, energies of different physical origins [23, 21, 11, 24], with the ratios of corresponding coupling constants determining the small “cutoff” length scale in the problem. Isometries of negatively curved surfaces have no small scale-cutoff, and for surfaces that are sufficiently large optimizing the bending energy among isometries naturally leads to distributed branch points.

As we discuss in the introduction, a commonly posited explanation for the fractal-like buckling patterns in hyperbolic sheets, is that the buckling manifests the competition between stretching and bending energies in the sheet. In this argument the non-existence and singularity theorems in [47, 48, 3, 27] are the primary sources for the intuition that even free hyperbolic sheets *have* to stretch. We argued in §1 that the theorems did not directly apply because we have bounded domains. This argument is true but still somewhat unsatisfactory. While it shows that smooth isometries are allowed, it does not explain the observed refinement of the buckling pattern as we approach the boundary.

What we therefore need are *quantitative* versions of the non-existence/singularity theorems, i.e. rather than statements that smooth isometries do not exist for the complete hyperbolic plane, we should address how the curvature grows as a function of R , for immersions, of a hyperbolic disk with radius R , in various regularity classes. The results in §3 and algorithms in §4 are steps towards this goal. We have numerical results as well as a (non-rigorous) scaling argument to show, for a disk of radius R and Gauss curvature $K = -1$ immersed in \mathbb{R}^3 , the maximum principal curvature κ_{max} grows as

$$(6.1) \quad \log(\kappa_{max}) \sim \begin{cases} R & C^2 \text{ or smoother isometries,} \\ \sqrt{R} & C^{1,1} \text{ branched isometries.} \end{cases}$$

The numerical evidence for these results is in Fig. 21a, and to be mathematically rigorous, what we have obtained are (numerical) upper bounds. Nonetheless, we think this is a remarkable result and that the corresponding lower bounds are also true.

This result underscores the importance of understanding the regularity of solutions, and the need to critically examine the superficially reasonable claim that “everything physical is smooth, so we lose nothing by assuming that the desired solution is smooth from the outset”. Arguably, it might be true that everything “physical” is smooth at some scale, and also discrete at an even smaller scale. So we can “use” smoothness only at the appropriate scales and only in the context of a “full” theory that includes the physics which enforces sufficient regularity for the solutions to be smooth.

For thin hyperbolic sheets, such theories include the full three dimensional elastic theory (2.1) or the finite thickness non-Euclidean plate theory (2.4), with $h > 0$. For these energy functionals, the sheet will develop narrow boundary layers, on a cutoff scale determined by the thickness and the size of the domain, and the solution is indeed smooth on this scale [37]. Numerical methods that rely on smoothness, for example finite difference methods that use a compact stencil to evaluate derivatives, will require a fine-scale discretization that resolves solutions at the scale of the smoothness.

On the other hand, “limit” theories, as in (2.5) or (3.1) for example, arise from sending the cutoff scale (here dependent on the thickness h) to zero. The corresponding limit solutions *need no longer be smooth*. This liberates us from the need to resolve the solution on a small-scale, and we are free to use a (relatively) coarse grid. The price we pay is that we now need specialized methods that can work with discontinuous functions and capture relevant ‘singular’ features of the limit solutions. This is the case for the DDG methods in §4 which work on somewhat coarse quadmeshes, but do explicitly encode the asymptotic skeleton S and the topological indices m_p at branch points.

While the topological charges m_p , or equivalently Δ in (3.22), concentrate on the branch points in the limit theories, a more accurate physical picture would spread them out over an appropriate core size. Ref. [2] outlines an approach, using additional fields (similar to gauge fields for defects [61]) to achieve this. Ref. [2] also outlines a continuum-mechanical formulation, based on thermodynamic principles, for modeling dynamical processes in hyperbolic sheets, including evolution of the prestrain (i.e. the intrinsic metric) and dynamics of (diffuse) branch point defects.

We view the conjecture in (6.1) as a ‘quantitative Hilbert theorem’. If true, it does explain why, for sufficiently large disks, isometries with distributed branch points are preferred. It gives a quantitative measure of the energy gap between smooth and branched isometries. The related argument for cut-depth indicates how the branch points will be distributed, and “explains” the observed self-similar buckling patterns in thin hyperbolic objects. Our goal for future work is to prove conjecture (6.1) rigorously and make a quantitative connection to the morphology of natural and engineered hyperbolic surfaces.

This work, although only an initial foray into the study of distributed branch points on hyperbolic surfaces (see also [36]), gives a glimpse of the breadth of this area, with question that touch upon analysis, geometry (discrete and continuous), topology, numerical methods, soft materials and mechanics. We view this work as just the tip of an iceberg, and we anticipate that it will spur further work, from mathematicians, physicists, engineers and artists, into the geometry, mechanics and control of branch points on hyperbolic surfaces.

APPENDIX A. ASYMPTOTICS OF PAINLEVÉ III

For $\varphi \ll 1$, the Painlevé III equation (5.3), and the associated boundary conditions, reduce to

$$\varphi''(z) + \frac{\varphi'(z)}{z} - \varphi(z) = 0, \quad \varphi(0) = \varphi_0, \quad \varphi'(0) = 0.$$

The solution is given by $\varphi(z) = \varphi_0 I_0(z)$, where I_0 is the modified Bessel function of the first kind [1, §9.6]. From the small and large z asymptotics of I_0 [1, §9.7], we get

$$\begin{aligned} \varphi_{\text{inner}}(z) &= \varphi_0 \left(1 + \frac{z^2}{4} + O(z^4) \right), \quad \text{for } z \ll 1, \\ \varphi_{\text{outer}}(z) &= \varphi_0 \frac{e^z}{\sqrt{2\pi z}} \left(1 + \frac{1}{8z} + O\left(\frac{1}{z^2}\right) \right), \quad \text{for } z \gg 1. \end{aligned}$$

For the regime $z \gg 1, \varphi \approx \pi$, we have the weakly damped pendulum equation:

$$(A.1) \quad \varphi''(z) - \sin \varphi(z) = -\frac{\varphi'(z)}{z} \approx 0,$$

with asymptotic solutions of the form

$$(A.2) \quad \varphi_{\text{pend}}(z) \approx \pi - A \sin(z^* - z),$$

for a slowly-varying amplitude A that changes over many cycles of the pendulum. We are only interested in the first crossing $\phi(z^*) = \pi$, so we can assume that A is constant and determine A by matching the large z asymptotics of the Bessel solution with the pendulum solution. From the Bessel solution, we derive initial data for the pendulum equation, fixing the energy level for this conservative system:

$$(A.3) \quad (\varphi_{\text{pend}}(0), \varphi'_{\text{pend}}(0)) \approx \left(\frac{\varphi_0 e^z}{\sqrt{2\pi z}}, \frac{\varphi_0 e^z}{\sqrt{2\pi z}} \right) = (\delta, \delta),$$

where we match at such a point z that $z \gg 1, \delta \ll 1$. The energy of the pendulum solution is given by

$$(A.4) \quad E = \frac{\varphi'^2}{2} + \cos \varphi \approx 1 + \frac{\delta^4}{24},$$

as $\cos \varphi$ is the potential and $\delta \ll 1$. Substituting the data into the energy we find

$$\begin{aligned} 1 + \frac{\delta^4}{24} &\approx \frac{1}{2} (A' \sin(z^* - z) + A \cos(z^* - z))^2 + \cos \varphi, \\ &\approx \frac{1}{2} (A' \sin(z^* - z) + A \cos(z^* - z))^2 - 1 + \frac{(\pi - \varphi)^2}{2}, \\ &\approx \frac{1}{2} (A' \sin(z^* - z) + A \cos(z^* - z))^2 - 1 + \frac{1}{2} A^2 \sin^2(z^* - z), \\ &\approx -1 \frac{1}{2} [A'^2 \sin^2(z^* - z) - 2A'A \sin(z^* - z) \cos(z^* - z) + A^2]. \end{aligned}$$

Which in the case of slowly varying A simplifies to

$$A \approx 2\sqrt{1 + \frac{\delta^4}{48}}.$$

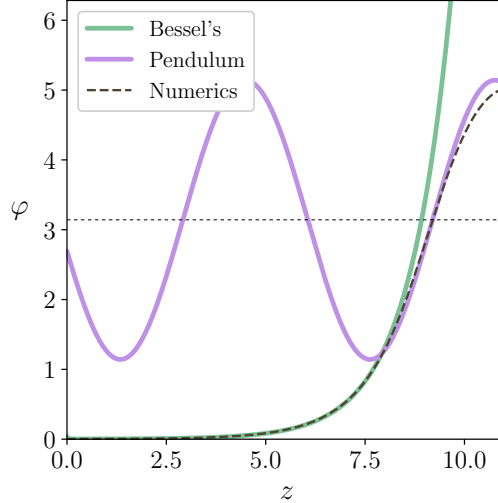


FIGURE 26. Asymptotics using the Pendulum and Bessel approximations in the $\varphi_0 \rightarrow 0$ limit compared to the numerical solution of the Painlevé equation for $\varphi_0 = \frac{\pi}{100}$. Our interest is in approximating the exact solution well on an interval $[0, z^*]$ where $z = z^* \approx 9$ is the first instance where $\varphi(z) = \pi$, depicted by the dashed horizontal line in the figure.

We are now equipped with a complete asymptotic description of the solutions to Painlevé III for an initial angle φ_0 . The description is divided into three regimes: $z \ll 1$ and $\varphi_0 \lesssim \varphi \ll \pi$, $z \gg 1$ and $\varphi_0 \ll \varphi \lesssim \pi$, and finally $z \gg 1$ and $\varphi \approx \pi$:

$$(A.5) \quad \varphi(z) \approx \begin{cases} \varphi_0 \left(1 + \frac{z^2}{4}\right), & z \ll 1 \text{ and } \varphi_0 \lesssim \varphi \ll \pi \\ \varphi_0 \frac{e^z}{\sqrt{2\pi z}} \left(1 + \frac{1}{8z}\right), & z \gg 1 \text{ and } \varphi_0 \ll \varphi \lesssim \pi \\ \pi - 2\sqrt{1 + \frac{e^{4z}}{192\pi^2 z^2}} \sin(z^* - z), & \varphi \approx \pi, z \lesssim z^* \approx -\log(\varphi_0) \end{cases}$$

A numerical validation of these asymptotic relations is illustrated in Fig. 26 (we consider $\varphi_0 = \frac{\pi}{100}$). We use the expressions in (A.5) to obtain the recursion relations (5.8), which are central to our analysis of the energy and cut-depth scaling in §5.1.

ACKNOWLEDGMENTS

We are grateful to Amit Acharya, Andrew Sageman-Furnas, David Glickenstein, Eran Sharon, John Gemmer and Kenneth Yamamoto for many stimulating discussions. SV gratefully acknowledges the hospitality of the Center for Nonlinear Analysis at Carnegie Mellon University, the Oxford Center for Industrial and Applied Math at Oxford University and the Hausdorff Institute at the University of Bonn where portions of this work were carried out. TS was partially supported by a Michael Tabor fellowship from the Graduate Interdisciplinary Program in Applied Mathematics at the University of Arizona. SV was partially supported by the Simons Foundation through awards 524875 and 560103 and partially supported by the NSF award DMR-1923922.

AUTHOR CONTRIBUTIONS

This article grew out of the Ph.D thesis work of TS under the supervision of SV. TS wrote the initial draft. SV revised the draft and incorporated additional material. Both authors contributed equally to performing the research reported here. Both authors read and approved the final manuscript.

REFERENCES

- [1] M. Abramowitz and I. A. Stegun, editors. *Handbook of mathematical functions with formulas, graphs, and mathematical tables*. Dover Publications Inc., New York, 1992. Reprint of the 1972 edition.
- [2] A. Acharya and S. C. Venkataramani. Mechanics of moving defects in growing sheets: 3-d, small deformation theory. *Materials Theory*, 4(1):2, 2020.
- [3] M.-H. Amsler. Des surfaces à courbure négative constante dans l'espace à trois dimensions et de leurs singularités. *Mathematische Annalen*, 130(3):234–256, 1955.
- [4] J. Anderson. *Hyperbolic geometry*. Springer, London New York, 2005.
- [5] R. Arora and A. Acharya. A unification of finite deformation J2 Von-Mises plasticity and quantitative dislocation mechanics. *Journal of the Mechanics and Physics of Solids*, page 104050, 2020.
- [6] A. Asratian. *Bipartite graphs and their applications*. Cambridge University Press, Cambridge U.K., New York, 1998.
- [7] B. Audoly and A. Boudaoud. ‘ruban à godets’: an elastic model for ripples in plant leaves. *Comptes Rendus Mécanique*, 330(12):831–836, 2002.

- [8] B. Audoly and A. Boudaoud. Self-similar structures near boundaries in strained systems. *Phys. Rev. Lett.*, 91(8):086105, 2003.
- [9] B. Audoly and Y. Pomeau. *Elasticity and geometry: from hair curls to the non-linear response of shells*. Oxford University Press, 2010.
- [10] P. Bella and R. V. Kohn. Metric-induced wrinkling of a thin elastic sheet. *J. Nonlinear Sci.*, 24(6):1147–1176, 2014.
- [11] P. Bella and R. V. Kohn. Wrinkles as the result of compressive stresses in an annular thin film. *Communications on Pure and Applied Mathematics*, 67(5):693–747, 2014.
- [12] M. Ben Amar and Y. Pomeau. Crumpled paper. *Proceedings of the Royal Society of London. Series A: Mathematical, Physical and Engineering Sciences*, 453(1959):729–755, 1997.
- [13] A. I. Bobenko and U. Eitner. *Painlevé equations in the differential geometry of surfaces*, volume 1753. Springer Science & Business Media, 2000.
- [14] A. I. Bobenko and R. Seiler. *Discrete integrable geometry and physics*. Number 16 in Oxford Lecture Series in Mathematics and Its Applications. Oxford University Press, USA, 1999.
- [15] A. I. Bobenko, J. M. Sullivan, P. Schröder, and G. M. Ziegler. *Discrete differential geometry*. Springer, 2008.
- [16] A. I. Bobenko and Y. B. Suris. Integrable systems on quad-graphs. *Int. Math. Res. Not.*, 2002(11):573–611, 2002.
- [17] A. I. Bobenko and Y. B. Suris. *Discrete differential geometry: Integrable structure*, volume 98 of *Graduate Studies in Mathematics*. American Mathematical Society, Providence, RI, 2008.
- [18] H. Brezis and L. Nirenberg. Degree theory and BMO. I. Compact manifolds without boundaries. *Selecta Math. (N.S.)*, 1(2):197–263, 1995.
- [19] H. Brezis and L. Nirenberg. Degree theory and BMO. II. Compact manifolds with boundaries. *Selecta Math. (N.S.)*, 2(3):309–368, 1996. With an appendix by the authors and Petru Mironescu.
- [20] E. Cerda, S. Chaieb, F. Melo, and L. Mahadevan. Conical dislocations in crumpling. *Nature*, 401:46–49, 1999.
- [21] J. Chopin, V. Démary, and B. Davidovitch. Roadmap to the morphological instabilities of a stretched twisted ribbon. *Journal of Elasticity*, 119(1-2):137–189, 2014.
- [22] P. G. Ciarlet. A justification of the von Kármán equations. *Archive for Rational Mechanics and Analysis*, 73(4):349–389, 1980.
- [23] B. Davidovitch, R. D. Schroll, D. Vella, M. Adda-Bedia, and E. A. Cerda. Prototypical model for tensional wrinkling in thin sheets. *Proceedings of the National Academy of Sciences*, 108(45):18227–18232, 2011.
- [24] B. Davidovitch, Y. Sun, and G. M. Grason. Geometrically incompatible confinement of solids. *Proceedings of the National Academy of Sciences*, 116(5):1483–1488, 2019.
- [25] J. F. Dorfmeister and I. Sterling. Pseudospherical surfaces of low differentiability. *Adv. Geom.*, 16(1):1–20, 2016.
- [26] N. V. Efimov. Impossibility of an isometric imbedding in Euclidean 3-space of certain manifolds with negative Gaussian curvature. *Dok. Akad. Nauk SSSR*, 146:296–299, 1962.
- [27] N. V. Efimov. Generation of singularities on surfaces of negative curvature. *Matematicheskii Sbornik*, 106(2):286–320, 1964.
- [28] E. Efrati, Y. Klein, H. Aharoni, and E. Sharon. Spontaneous buckling of elastic sheets with a prescribed non-Euclidean metric. *Physica D: Nonlinear Phenomena*, 235(1):29–32, 2007.
- [29] E. Efrati, E. Sharon, and R. Kupferman. Elastic theory of unconstrained non-Euclidean plates. *Journal of the Mechanics and Physics of Solids*, 57(4):762–775, 2009.
- [30] E. Efrati, E. Sharon, and R. Kupferman. The metric description of elasticity in residually stressed soft materials. *Soft Matter*, 9(34):8187–8197, 2013.
- [31] L. P. Eisenhart. *A treatise on the differential geometry of curves and surfaces*. Ginn, 1909.
- [32] L. C. Evans. *Partial differential equations*. American Mathematical Society, 1998.

- [33] A. Fathi, F. Laudenbach, and V. Poénaru. *Thurston's work on surfaces*, volume 48 of *Mathematical Notes*. Princeton University Press, Princeton, NJ, 2012. Translated from the 1979 French original by Djun M. Kim and Dan Margalit.
- [34] G. Friesecke, R. D. James, and S. Müller. The Föppl–von Kármán plate theory as a low energy Γ -limit of nonlinear elasticity. *Comptes Rendus Mathématique*, 335(2):201–206, 2002.
- [35] G. Friesecke, R. D. James, and S. Müller. A hierarchy of plate models derived from nonlinear elasticity by Gamma-convergence. *Archive for rational mechanics and analysis*, 180(2):183–236, 2006.
- [36] J. Gemmer, E. Sharon, T. Shearman, and S. C. Venkataramani. Isometric immersions, energy minimization and self-similar buckling in non-Euclidean elastic sheets. *Europhys. Lett.*, 114(2):24003, 2016.
- [37] J. Gemmer and S. Venkataramani. Defects and boundary layers in non-euclidean plates. *Nonlinearity*, 25(12):3553, 2012.
- [38] J. A. Gemmer and S. C. Venkataramani. Shape selection in non-Euclidean plates. *Physica D: Nonlinear Phenomena*, 240(19):1536–1552, 2011.
- [39] J. A. Gemmer and S. C. Venkataramani. Defects and boundary layers in non-Euclidean plates. *Nonlinearity*, 25(12):3553–3581, 2012.
- [40] J. A. Gemmer and S. C. Venkataramani. Shape transitions in hyperbolic non-Euclidean plates. *Soft Matter*, 9(34):8151–8161, 2013.
- [41] J. Guven, M. M. Müller, and P. Vázquez-Montejo. Isometric bending requires local constraints on free edges. *Mathematics and Mechanics of Solids*, 24(12):4051–4077, 2020/06/26 2019.
- [42] Q. Han and J.-X. Hong. *Isometric Embedding of Riemannian manifolds in Euclidean spaces*, volume 130. American Mathematical Society Providence, RI, 2006.
- [43] P. Hartman and L. Nirenberg. On spherical image maps whose Jacobians do not change sign. *Amer. J. Math.*, 81:901–920, 1959.
- [44] P. Hartman and A. Wintner. On the asymptotic curves of a surface. *American Journal of Mathematics*, 73(1):149–172, 1951.
- [45] A. Hatcher. *Algebraic topology*. Cambridge University Press, Cambridge, 2002.
- [46] D. W. Henderson and D. Taimina. Crocheting the hyperbolic plane. *The Mathematical Intelligencer*, 23(2):17–28, 2001.
- [47] D. Hilbert. Über Flächen von constanter Gaussscher Krümmung. *Transactions of the American Mathematical Society*, 2(1):87–99, 1901.
- [48] E. Holmgren. Sur les surfaces à courbure constante négative. *CR Acad. Sci. Paris*, 134:740–743, 1902.
- [49] J. X. Hong. Realization in \mathbf{R}^3 of complete Riemannian manifolds with negative curvature. *Comm. Anal. Geom.*, 1(3-4):487–514, 1993.
- [50] C. Huang, Z. Wang, D. Quinn, S. Suresh, and K. J. Hsia. Differential growth and shape formation in plant organs. *Proceedings of the National Academy of Sciences*, 115(49):12359–12364, 2018.
- [51] E. Huhnen-Venedey and T. Rörig. Discretization of asymptotic line parametrizations using hyperboloid surface patches. *Geometriae Dedicata*, 168(1):265–289, 2014.
- [52] G.-O. Ishikawa and Y. Machida. Singularities of improper affine spheres and surfaces of constant Gaussian curvature. *Internat. J. Math.*, 17(3):269–293, 2006.
- [53] T. A. Ivey and J. Landsberg. *Cartan for beginners*, volume 61 of *Graduate Studies in Mathematics*. American Mathematical Society Providence, RI, 2003.
- [54] T. Kaczynski, K. Mischaikow, and M. Mrozek. *Computational homology*, volume 157 of *Applied Mathematical Sciences*. Springer-Verlag, New York, 2004.
- [55] J. Kim, J. A. Hanna, M. Byun, C. D. Santangelo, and R. C. Hayward. Designing responsive buckled surfaces by halftone gel lithography. *Science*, 335(6073):1201–1205, 2012.
- [56] J. Kim, J. A. Hanna, R. C. Hayward, and C. D. Santangelo. Thermally responsive rolling of thin gel strips with discrete variations in swelling. *Soft Matter*, 8(8):2375–2381, 2012.
- [57] S. Kim, C. Laschi, and B. Trimmer. Soft robotics: a bioinspired evolution in robotics. *Trends in biotechnology*, 31(5):287–294, 2013.
- [58] B. Kirchheim. *Rigidity and Geometry of Microstructures*. Habilitation, University of Leipzig, 2001.

- [59] Y. Klein, E. Efrati, and E. Sharon. Shaping of elastic sheets by prescription of non-Euclidean metrics. *Science*, 315(5815):1116–1120, 2007.
- [60] Y. Klein, S. Venkataramani, and E. Sharon. Experimental Study of Shape Transitions and Energy Scaling in Thin Non-Euclidean Plates. *Phys. Rev. Lett.*, 106(11):118303, March 2011.
- [61] H. Kleinert. *Gauge fields in condensed matter. Vol II: Stresses and Defects*. World Scientific, Singapore Teaneck, N.J, 1989.
- [62] N. H. Kuiper. On C^1 -isometric imbeddings. I, II. *Nederl. Akad. Wetensch. Proc. Ser. A*. **58** = *Indag. Math.*, 17:545–556, 683–689, 1955.
- [63] M. Lewicka, L. Mahadevan, and M. R. Pakzad. The Föppl-von Kármán equations for plates with incompatible strains. *Proc. Roy. Soc. London Ser. A*, 467(2126):402–426, 2011.
- [64] M. Lewicka and M. Reza Pakzad. Scaling laws for non-Euclidean plates and the $w_{\{2,2\}}$ isometric immersions of Riemannian metrics. *ESAIM: Control, Optimisation and Calculus of Variations*, 17(04):1158–1173, 2011.
- [65] H. Liang and L. Mahadevan. The shape of a long leaf. *Proceedings of the National Academy of Sciences*, 106(52):22049–22054, 2009.
- [66] H. Liang and L. Mahadevan. Growth, geometry, and mechanics of a blooming lily. *Proceedings of the National Academy of Sciences*, 108(14):5516–5521, April 2011.
- [67] A. Lobkovsky, S. Gentges, H. Li, D. Morse, and T. A. Witten. Scaling properties of stretching ridges in a crumpled elastic sheet. *Science*, 270:1482, 1995.
- [68] J. Louis-Rosenberg. Floraform. <http://n-e-r-v-o-u-s.com/blog/?p=6721>, 2014 (accessed June 21, 2020).
- [69] A. E. H. Love. *A treatise on the mathematical theory of elasticity*. Cambridge university press, 1892.
- [70] M. Marder, E. Sharon, S. Smith, and B. Roman. Theory of edges of leaves. *EPL (Europhysics Letters)*, 62(4):498, 2003.
- [71] G. Meyer. 2013 bridges conference: Mathematical art galleries. http://gallery.bridgesmathart.org/exhibitions/2013-bridges-conference/gabriele_meyer, 2013 (accessed June 21, 2020).
- [72] T. K. Milnor. Efimov’s theorem about complete immersed surfaces of negative curvature. *Advances in Math.*, 8(3):474–543, 1972.
- [73] S. Müller. Mathematical problems in thin elastic sheets: Scaling limits, packing, crumpling and singularities. In J. Ball and P. Marcellini, editors, *Vector-Valued Partial Differential Equations and Applications: Cetraro, Italy 2013*, pages 125–193. Springer International Publishing, Cham, 2017.
- [74] J. Nash. C^1 isometric imbeddings. *Annals of mathematics*, pages 383–396, 1954.
- [75] S. Nechaev and K. Polovnikov. From geometric optics to plants: the eikonal equation for buckling. *Soft Matter*, 13:1420–1429, 2017.
- [76] S. Nechaev and R. Voituriez. On the plant leaf’s boundary, jupe à godets’ and conformal embeddings. *J. Phys. A: Mathematical and General*, 34(49):11069, 2001.
- [77] H. Olbermann. The one-dimensional model for d-cones revisited. *Adv. Calc. Var.*, 9(3):201–215, 2016.
- [78] V. Poénaru. Some aspects of the theory of defects of ordered media and gauge fields related to foliations. *Communications in Mathematical Physics*, 80(1):127–136, 1981.
- [79] C. Rogers and W. K. Schief. *Bäcklund and Darboux transformations: geometry and modern applications in soliton theory*, volume 30. Cambridge University Press, 2002.
- [80] E. R. Rozendorn. On complete surfaces of negative curvature $K \leq -1$ in the Euclidean spaces E_3 and E_4 . *Mat. Sb. (N.S.)*, 58 (100):453–478, 1962.
- [81] E. R. Rozendorn. Properties of asymptotic lines on surfaces with slowly varying negative curvature. *Dokl. Akad. Nauk SSSR*, 145:538–540, 1962.
- [82] E. R. Rozendorn. Weakly irregular surfaces of negative curvature. *Uspehi Mat. Nauk*, 21(5 (131)):59–116, 1966.
- [83] E. R. Rozendorn. Surfaces of Negative Curvature. In Y. D. Burago and V. A. Zalgaller, editors, *Geometry III*, volume 48 of *Encyclopaedia of Mathematical Sciences*, pages 87–178. Springer Berlin Heidelberg, 1992.

- [84] R. Sauer. Parallelogrammgitter als Modelle pseudosphärischer Flächen. *Mathematische Zeitschrift*, 52(1):611–622, 1950.
- [85] E. Sharon, M. Marder, and H. L. Swinney. Leaves, flowers and garbage bags: making waves. *American Scientist*, 92(3):254, 2004.
- [86] E. Sharon, B. Roman, M. Marder, G.-S. Shin, and H. L. Swinney. Buckling cascades in free sheets. *Nature*, 419(6907):579–579, 2002.
- [87] E. Sharon, B. Roman, and H. L. Swinney. Geometrically driven wrinkling observed in free plastic sheets and leaves. *Physical Review E (Statistical, Nonlinear, and Soft Matter Physics)*, 75(4):046211, 2007.
- [88] E. Sharon and M. Sahaf. The mechanics of leaf growth on large scales. In A. Geitmann and J. Gril, editors, *Plant Biomechanics: From Structure to Function at Multiple Scales*, pages 109–126. Springer International Publishing, 2018.
- [89] J. J. Stoker. *Differential geometry*. Wiley Classics Library. John Wiley & Sons Inc., 1989. Reprint of the 1969 original, A Wiley-Interscience Publication.
- [90] G. I. Taylor. The mechanism of plastic deformation of crystals. Part I: Theoretical. *Proceedings of the Royal Society of London. Series A, Containing Papers of a Mathematical and Physical Character*, 145(855):362–387, 1934.
- [91] W. P. Thurston. On the geometry and dynamics of diffeomorphisms of surfaces. *Bull. Amer. Math. Soc. (N.S.)*, 19(2):417–431, 1988.
- [92] S. C. Venkataramani. Lower bounds for the energy in a crumpled elastic sheet—a minimal ridge. *Nonlinearity*, 17(1):301, 2003.
- [93] R. Vetter, N. Stoop, T. Jenni, F. K. Wittel, and H. J. Herrmann. Subdivision shell elements with anisotropic growth. *International Journal for Numerical Methods in Engineering*, 95(9):791–810, 2013.
- [94] T. Weinstein. *An introduction to Lorentz surfaces*, volume 22 of *De Gruyter Expositions in Mathematics*. Walter de Gruyter & Co., Berlin, 1996.
- [95] M. Wertheim. Corals, crochet and the cosmos: how hyperbolic geometry pervades the universe. <https://theconversation.com/corals-crochet-and-the-cosmos-how-hyperbolic-geometry-pervades-the-universe-53382>, 2016 (accessed June 21, 2020).
- [96] M. Wertheim and C. Wertheim. *Crochet Coral Reef*. Institute for Figuring, Los Angeles, 2015. With contributions by Leslie Dick, Marion Endt-Jones and Anna Mayer and a foreword by Donna Haraway.
- [97] W. S. Wong and A. Salleo. *Flexible electronics: materials and applications*, volume 11. Springer Science & Business Media, 2009.
- [98] W. Wunderlich. Zur Differenzengeometrie der Flächen konstanter negativer Krümmung. *Österreich. Akad. Wiss. Math.-Nat. Kl. S.-B. Ila.*, 160:39–77, 1951.

PROGRAM IN APPLIED MATHEMATICS, 627 N. SANTA RITA AVENUE, UNIVERSITY OF ARIZONA, TUCSON, AZ 85721

E-mail address: toby.shearman@gmail.com

DEPARTMENT OF MATHEMATICS, 627 N. SANTA RITA AVENUE, UNIVERSITY OF ARIZONA, TUCSON, AZ 85721

E-mail address: shankar@math.arizona.edu